Two warm Neptunes transiting HIP 9618 revealed by TESS and Cheops

Osborn, H.P.; Nowak, G.; Hébrard, G.; Masseron, T.; Lillo-Box, J.; Pallé, E.; ... ; Winn, J.N.

Two warm Neptunes transiting HIP 9618 revealed by *TESS* and *Cheops*

H. P. Osborn [1,2]★ G. Nowak [3,4,5] G. Hébrard [6] T. Masseron [4,5] J. Lillo-Box [7] E. Pallé [4,5]
A. Bekkelien,[8] H.-G. Florén,[9] P. Guterman,[10] A. E. Simon [1] V. Adibekyan [11] A. Bieryla [12]
L. Borsato [13] A. Brandeker [9] D. R. Ciardi [14] A. Collier Cameron,[15] K. A. Collins [12]
J. A. Egger [1] D. Gandolfi [16] M. J. Hooton [1,17] D. W. Latham [12] M. Lendl [8] E. C. Matthews [8,18]
A. Tuson [17] S. Ulmer-Moll [8] A. Vanderburg [2] T. G. Wilson [15] C. Ziegler,[19] Y. Alibert [1]
R. Alonso [4,5] G. Anglada [20,21] L. Arnold,[22] J. Asquier,[23] D. Barrado y Navascues,[24]
W. Baumjohann [25] T. Beck [1] A. A. Belinski [26] W. Benz [1,27] F. Biondi [13,28] I. Boisse [10]
X. Bonfils [29] C. Broeg [1,27] L. A. Buchhave [30] T. Bárczy [31] S. C. C. Barros [32,33] J. Cabrera [34]
C. Cardona Guillen,[4,5] I. Carleo,[4,5] A. Castro-González [7] S. Charnoz [35] J. Christiansen,[14]
P. Cortes-Zuleta [10] S. Csizmadia [34] S. Dalal,[6] M. B. Davies [36] M. Deleuil [10] X. Delfosse,[37]
L. Delrez [38,39] B.-O. Demory [40] A. B. Dunlavey,[14] D. Ehrenreich [8] A. Erikson,[34]
R. B. Fernandes [41] A. Fortier [1,27] T. Forveille,[37] L. Fossati [25] M. Fridlund [42,43] M. Gillon [38]
R. F. Goeke,[2] M. V. Goliguzova [26] E. J. Gonzales [44] M. N. Günther [23] M. Güdel [45] N. Heidari,[10]
C. E. Henze,[46] S. Howell,[46] S. Hoyer [10] J. I. Frey,[40] K. G. Isaak [23] J. M. Jenkins [46] F. Kiefer,[6,47]
L. Kiss,[48,49] J. Korth,[50,51] P. F. L. Maxted,[52] J. Laskar [53] A. Lecavelier des Etangs [54] C. Lovis [8]
M. B. Lund [14] R. Luque,[55] D. Magrin [13] J. M. Almenara [37] E. Martioli,[6,56] M. Mecina,[45]
J. V. Medina,[57] D. Moldovan,[58] M. Morales-Calderón,[7] G. Morello,[4,5] C. Moutou,[59] F. Murgas,[4,5]
E. L. N. Jensen [60] V. Nascimbeni [13] G. Olofsson [9] R. Ottensamer,[45] I. Pagano [61] G. Peter [34]
G. Piotto [13,62] D. Pollacco,[63] D. Queloz [64,65] R. Ragazzoni [13,62] N. Rando,[23] H. Rauer [34,66,67]
I. Ribas [20,21] G. Ricker [2] O. D. S. Demangeon [32,33] A. M. S. Smith [34] N. Santos [32,33]
G. Scandariato [61] S. Seager [2] S. G. Sousa [32] M. Steller [25] G. M. Szabó [68,69] D. Ségransan [8]
N. Thomas,[1] S. Udry [8] B. Ulmer,[70] V. Van Grootel [39] R. Vanderspek [2] N. Walton [71]
and J. N. Winn [72]

Affiliations are listed at the end of the paper

ABSTRACT

HIP 9618 (HD 12572, TOI-1471, TIC 306263608) is a bright ($G = 9.0$ mag) solar analogue. *TESS* photometry revealed the star to have two candidate planets with radii of $3.9 \pm 0.044 R_\oplus$ (HIP 9618 b) and $3.343 \pm 0.039 R_\oplus$ (HIP 9618 c). While the 20.77291 d period of HIP 9618 b was measured unambiguously, HIP 9618 c showed only two transits separated by a 680-d gap in the time series, leaving many possibilities for the period. To solve this issue, *CHEOPS* performed targeted photometry of period aliases to attempt to recover the true period of planet c, and successfully determined the true period to be 52.56349 d. High-resolution spectroscopy with *HARPS-N*, *SOPHIE*, and *CAFE* revealed a mass of $10.0 \pm 3.1 M_\oplus$ for HIP 9618 b, which, according to our interior structure models, corresponds to a 6.8 ± 1.4 per cent gas fraction. HIP 9618 c appears to have a lower mass than HIP 9618 b, with a 3-sigma upper limit of $<18 M_\oplus$. Follow-up and archival RV measurements also reveal a clear long-term trend which, when combined with imaging and astrometric information, reveal a low-mass companion ($0.08^{+0.12}_{-0.05} M_\odot$) orbiting at $26.0^{+19.0}_{-11.0}$ au. This detection makes HIP 9618 one of only five bright ($K < 8$ mag) transiting multiplanet systems known to host a planet with $P > 50$ d, opening the door for the atmospheric characterization of warm ($T_{eq} < 750$ K) sub-Neptunes.

Key words: surveys – eclipses – occultations – planets and satellites: detection – binaries: spectroscopic.

★ E-mail: hugh.osborn@space.unibe.ch

1 INTRODUCTION

The detection and characterization of transiting exoplanets is currently the main driving force behind our rapidly expanding knowledge of exoplanets and exoplanetary systems. This is in part driven by the expanding capability to perform precise transmission spectroscopy, especially with *JWST* (e.g. The JWST Transiting Exoplanet Community Early Release Science Team 2023). The ability of the *Transiting Exoplanet Survey Satellite* (*TESS*; Ricker et al. 2015) to find planets around bright stars has also greatly contributed, with *TESS* tripling the number of confirmed transiting planets around bright ($K < 8$) stars.[1]

Since the majority of the sky is covered by *TESS* with only 27-d sectors, many long-period planets escape detection. However, such planets are important. They are the ones least influenced by their parent stars, and therefore may maintain more primordial characteristics than their shorter period siblings (Owen 2019). Their cooler atmospheres may permit the detection of different atmospheric molecules. And their large Hill spheres mean these are the planets most likely to have stable moon or ring systems (e.g. Dobos et al. 2021). Therefore, confirming longer period transiting planets is key to expanding our knowledge of planetary formation and evolution and bridging the gap between Hot Jupiters and extrasolar systems more akin to the solar system.

While in much of the sky *TESS* is unable to catch consecutive transits of planets with orbital periods longer than 27 d, it is able to observe the planetary transits of such planets – either as single transits, or as non-consecutive 'duotransits'. In the case of these duotransiting planets, which are being found in abundance during *TESS*' extended mission, we typically have a two year gap between transits. Such cases are easier to solve than single transits as with two observed transits, the orbital period is limited to a discrete set of possible aliases. These can then either be searched using photometry or reduce the radial velocity phase space to specific periods. This technique has proved extremely fruitful in the *TESS* extended mission, with detections of the periods of i.e. TOI-2257 (Schanche et al. 2022), and TOIs 5152b & 5153b (Ulmer-Moll et al. 2022).

While giant duotransiting planets can typically be redetected with ground-based photometry, for super-Earths and mini-Neptunes which produce only shallow transits, targeted space-based photometry is the more reliable way to redetect such a transit. ESA's *CHEOPS* mission, a 30 cm space telescope in low-Earth orbit and specifically designed for transit photometry, is the perfect instrument for this task. CHEOPS observations thus far been useful to reveal the true periods of warm mini-Neptunes, including TOI-2076 c & d (Osborn et al. 2022), TOI-5678 b (Ulmer-Moll et al. 2023), HD 15906 c (Tuson et al. 2023), and HD 22946 d (Garai et al. 2023).

In this paper, we report the discovery of a transiting multiplanet and multistar system orbiting the bright ($G = 9.0$, $K = 7.8$) solar-like star HIP 9618. In Section 2 we summarize the various data taken from HIP 9618, including survey observations and targeted follow-up. In Section 3 we describe the analyses performed, including the derived stellar parameters and the final combined model used to derive planetary parameters. Sections 4 and 5 discuss the HIP 9618 system in context of the known exoplanetary systems and concludes.

---

[1]70/107 planets with $K < 8$ (https://exoplanetarchive.ipac.caltech.edu; accessed 2022 July 8; Akeson et al. 2013)

2 DATA DESCRIPTION

2.1 *TESS* and identification of two planetary signals

HIP 9618 was initially observed by *TESS* in sector 17 (Oct 2019) at 2-min cadence. The data were processed by the *TESS* science processing operations center (SPOC; Jenkins et al. 2016), which included aperture photometry, flagging poor-quality data, removal of trends associated with systematic and non-stellar sources (pre-search data conditioning; Stumpe et al. 2012, 2014; Smith et al. 2012) and finally a search for transiting exoplanets (Jenkins 2002; Jenkins et al. 2010, 2020). SPOC processing revealed a threshold-crossing event – i.e. a candidate planet – which passed all Data Validation checks (Twicken et al. 2018; Li et al. 2019) and was subsequently manually vetted by a team of astronomers as *TESS* Object of Interest 1471.01 (Guerrero et al. 2021). This initial candidate was the result of two transits seen in the S17 data, which were separated by 11.8 d – the purported initial TOI period.

As with all TOIs, the target was passed to various groups in the *TESS* Follow-up Observing Program (TFOP) with the task of taking complementary observations to help confirm the candidate as a bona fide planet. This included low-resolution spectroscopy to rule out large RV variations of an eclipsing binary as well as improving stellar parameters (see 2.4.2 and 2.4.1), high-resolution imaging to identify close-in blended stars which may be the source of the observed transits (see A0.1, A0.2, A0.3, & A0.4), and ground-based photometry to confirm the purported ephemeris and detect if its source is associated with the target star or a blended object (see 2.2).

Intriguingly, follow-up photometry with LCOGT at 11.8 d appeared to not reveal a transit at the TOI period as described in Section 2.2. Although this could have been a sign of Transit Timing Variations (TTVs) or even a blended source, this inspired a detailed inspection of the *TESS* light curve. This analysis revealed that the two transits in fact had different depths and durations, as well as finding a third transit in the S17 data which was present in the raw flux data but had been masked out during PDC detrending. This extra transit was not consistent with the 11.8 d TOI period, but was consistent in depth and duration with the initial transit, suggesting a ∼21 d period. In this scenario the second transit seen in the original *TESS* light-curve analysis was likely a monotransit from an outer planet orbiting HIP 9618.

TESS subsequently observed HIP 9618 during the Ecliptic campaign in sectors 42 & 43 (2021 August 20–October 12). TESS full-frame image (FFI) data were initially reduced and processed by the Quick-Look Pipeline (QLP), which runs a complementary photometric extraction, detrending and transit search (Huang et al. 2020). *TESS* data revealed a further three transits which QLP was able to use to detect the true period of TOI-1471.01 as 20.77291 d. After masking those transit events, QLP also detected a second transit of the outer planet candidate. This became TOI-1471.02. SPOC processing also revealed the true period of TOI-1471.01 when later processing S42 and S43 data.

2.1.1 Custom TESS detrending

In order to reveal the third transit in the S17 data, we re-extracted aperture photometry from the available *TESS* data and performed a custom detrending. Starting from the *TESS* 2-min-cadence target pixel files, we extracted light curves from 20 different photometric apertures. For each light curve, we fit a model to the time series consisting of a linear combination of a basis spline (with breakpoints spaced every 1.5 d to model long time-scale instrumental effects and

stellar variability) and systematics parameters relating to the means and standard deviations of the spacecraft quaternion time series (and the squared time series) within each exposure (see Vanderburg et al. 2019). Using a linear least-squares technique (matrix inversion), we solved for the best-fitting coefficients of our free parameters while iteratively excluding 3σ outliers from the fit until it reached convergence. After calculating the best-fitting systematics model for each aperture's light curve, we then subtracted it from the uncorrected light curve and identified the aperture that produced the light curve with the lowest photometric scatter. The best-performing aperture was roughly circular with a radius of about 3 pixels. For this aperture, we calculated the contribution of flux from stars other than the target and found that contamination was negligible (less than 0.5 per cent, much smaller than the uncertainty on the planet's transit depth) so we did not apply a correction for diluting flux.

2.2 LCOGT

Ground-based photometry was performed using the Las Cumbres Observatory Global Telescope (LCOGT; Brown et al. 2013). The first observation was performed using the 1.0 m node at McDonald Observatory on UTC 2020 January 13 to follow-up the ingress of the initially proposed orbital period of TOI-1471.01 at 11.767 d. Two later observations were performed on the nights of UTC 2022 September 4 and 8 with the 1.0 m telescopes at CTIO and SAAO, respectively, in order to confirm the periods found by *TESS* and *CHEOPS* observations.

All time series used the Pan-STARRS z-short band and used the `TESS Transit Finder`, which is a customized version of the `Tapir` software package (Jensen 2013), to schedule our transit observations. The 1 m telescopes are equipped with 4096 × 4096 SINISTRO cameras having an image scale of 0″389 per pixel, resulting in a 26 arcmin × 26 arcmin field of view. The images were calibrated by the standard LCOGT `BANZAI` pipeline (McCully et al. 2018). The telescopes were moderately defocused to attempt to improve photometric precision resulting in typical TOI-1471 full-width at half-maximum (FWHM) of 3″7. Photometric data were extracted using `AstroImageJ` (Collins et al. 2017) and circular photometric apertures with radii 7″0. The TOI-1471 photometric aperture included most of the flux of the delta *TESS* magnitude 7.382 *Gaia* eDR3 neighbour 3″35 southwest of TOI-1471.

In the case of the 2020 observation, the LCOGT light curve ruled out the expected 1.6 ppt egress in the TOI-1471 aperture as shown in Fig. 1. The LCOGT data also ruled out egress events deep enough to cause the signal in the *TESS* data in all four other *Gaia* neighbours within 2′5 of TOI-1471 that are bright enough to be capable of causing the *TESS* detection. The combination of results ruled out the initial TOI-1471.01 orbital period of 11.767 d, which prompted us to further investigate the events in the *TESS* data. For the 2022 observations, a simple transit model combined with decorrelation for simple metadata such as airmass & PSF FWHM reveals strong evidence for transits at the purported orbits (see Fig. 2).

2.3 CHEOPS

CHEOPS is a 30-cm ESA space telescope devoted to the characterization of exoplanets from its position in a sun-synchronous low-Earth orbit (Benz et al. 2021). HIP 9618 was observed on four occasions through *CHEOPS* GTO programme #48 'Duos: Recovering long period duotransiting planets with *CHEOPS*' in an attempt to recover the true period of HIP 9618 c. Four visits were scheduled (see Table 1), each with a duration of 7.1 *CHEOPS* orbits (11.85hr) and an
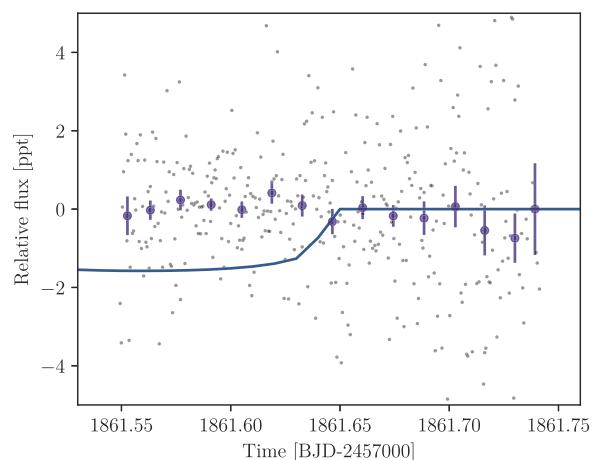

Figure 1. LCOGT photometry from the 1-m telescope at McDonald Observatory in 2020 which ruled out the 11.767 d period initially detected for TOI-1471.01. The grey points show individual points, purple circles show binned photometry (and errors), and the blue line represents the expected transit model given the initial TOI data.
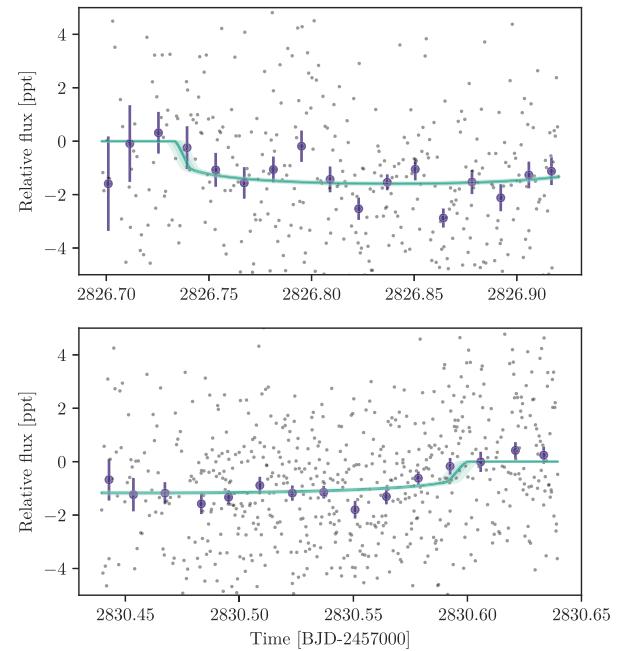

Figure 2. 2022 observations of HIP 9618 using LCOGT 1-m telescopes at CTIO and SAAO, respectively, which confirmed the orbital periods proposed here. Upper: Ingress of HIP 9618 b; Lower: Egress of HIP 9618 c. The grey points show individual points, circles show binned photometry (and errors), and the green line represents the expected transit model given priors from our final combined model.

exposure time of 46.65 s. The data for the first three *CHEOPS* visits is shown in Fig. 4. We used the `make_xml_files` function of `pycheops` (Maxted et al. 2022) to generate the visits and exposure time.

2.3.1 PIPE

We extracted photometry from the CHEOPS data by modelling the Point Spread Function (PSF) using the custom 'PSF imagette

Table 1. Key information for the *CHEOPS* photometry presented in this paper. The raw and detrended *CHEOPS* photometry shown in this paper is available on Vizier.

Start time (UT & BJD)	Dur (h)	Aliases (d)	File ref.
2021/11/24 04:37:17 2459542.69256	11.501	40.20d	CH_PR110048_TG017601_V0200
2021/12/04 20:39:18 2459553.36063	11.578	45.56 & 22.78d	CH_PR110048_TG017401_V0200
2021/12/11 08:47:17 2459559.86617	10.515	97.62, 48.81 & 24.40	CH_PR110048_TG017301_V0200
2021/12/18 22:42:58 2459567.44651	11.578	52.56d	CH_PR110048_TG017201_V0200

photometric extraction' (`PIPE`) package[2], which has also been used in past *CHEOPS* analyses (e.g. Szabó et al. 2022; Serrano et al. 2022). This uses the smaller but shorter cadence imagettes and a measured PSF template to measure the underlying stellar flux variations. Comparison with the CHEOPS DRP (Hoyer et al. 2020) reveals similar photometric precision, but with less severe trends as a function of e.g. roll angle. Hence we chose to use the PIPE photometry. PIPE is also able to use a map of detector hot pixels to remove noise due to variable hot pixels in the region of the PSF. It also applies a non-linearity correction to the background which reduces the number of outliers. To model the HIP 9618 imagettes we used a PSF model derived for HD 209458, which differs in $T_{\rm eff}$ by only 400 K and was observed at the same pixel location.

2.3.2 Analysis of period aliases

In order to assess the ability of *CHEOPS* to observe period aliases of HIP 9618 c, we performed an initial analysis using `MonoTools` (Osborn 2022) with the *TESS* data alone. This is an open-source transit-fitting package designed specifically for planets on long period orbits which produce only one or two transits. In the case of a so-called *duotransit* like HIP 9618 c – i.e. a transiting planet candidate with two observed transit but multiple possible period aliases – `MonoTools` takes care to calculate a precise period probability distribution.

The fitting process for duotransits is further described in Osborn et al. (2022), but we briefly explain it here. First, we simultaneously fit the inner periodic planet, and the two transits of the outer planet using the `exoplanet` package (Foreman-Mackey et al. 2021) – this ensures that any constraints from the inner planet on e.g. stellar density can help further constrain the outer body. For the duotransit candidate, we use the available *TESS* photometry to calculate the possible array of unobserved period aliases. In the case of HIP 9618 c there are 23 possible solutions. Unlike the inner planet, the duotransit is fitted using the transit shape alone (i.e. a way that is agnostic of orbital period) as well as using the central time of transit for each of the two transits. The resulting shape parameters constrain the transverse velocity of HIP 9618 c across the star.

To assess the marginalized probability across all period aliases, we can use all available information to produce constraining priors. First, we consider a simple period prior which incorporates the window function (i.e. given some observation τ, the probability of observing transits during that window decreases with τ/P, i.e. $p \propto P^{-1}$) and a factor to account for the fact that planetary occurrence is roughly uniform in $\log P$ rather than P, again meaning $p \propto P^{-1}$. These are detailed in Kipping (2018). Next we include a geometric prior – i.e. transit probability is inversely proportional to the distance during transit: $p \propto a_0/R_s$.
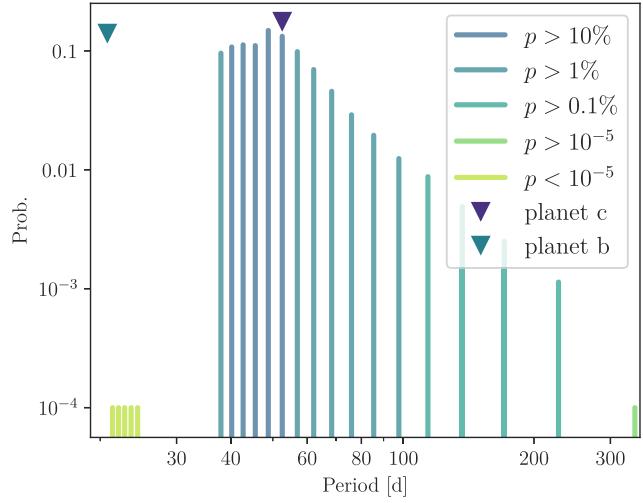
Figure 3. Marginalized probabilities for each of the period aliases of HIP 9618 c as calculated by `MonoTools`. The green bars for the period aliases <30 d are simply representative – these aliases actually have probabilities <10^{-45}.

We also have knowledge of the expected eccentricity of HIP 9618 c, both due to internal constraints within the planetary system (i.e. we know that its orbit cannot graze its host star or cross the orbit of HIP 9618 b), and also from the average distributions of exoplanetary eccentricities. For the former maximum eccentricity, we use the hill sphere of HIP 9618 b (assuming the average mass for its radius) to compute a maximum eccentricity for each potential period alias. For the latter population distribution, we use the eccentricity distribution of Van Eylen et al. (2019) to constrain the expected eccentricity of HIP 9618 c. Due to the form of the eccentricity distributions and the distribution of possible eccentricities (e), argument of periasteron (ω) for each transverse velocity ($v/v_{\rm circ}$), there is no analytical solution for this calculation, therefore we used 1.3×10^8 samples in $v/v_{\rm circ}$ and ω space to create 2D interpolated distributions of the prior probability as a function of both $v/v_{\rm circ}$ and $e_{\rm max}$.

We then combine all priors for each period alias and normalize the sum of the combined probabilities to 1, allowing us to assign marginal probabilities to each alias. We then sampled the fit using the Hamiltonian Monte Carlo sampler implemented in `PyMC3` (Salvatier et al. 2016) for 6000 steps across 6 chains, producing thousands of independent and well-mixed samples ($\hat{r} < 1.05$).

The result can be seen in Fig. 3. Due to our eccentricity prior eliminating aliases with orbits that are highly likely to cross that of HIP 9618 b, the five aliases between 21.35 and 24.40 d were excluded. Instead, the model showed a clear peak on periods of 40–60 d, with the average period across all aliases weighted by probability being 52.5 ± 14.6 d. We also inspected Keck/HIRES and Lick/APF RVs taken by the TKS group, however these did not
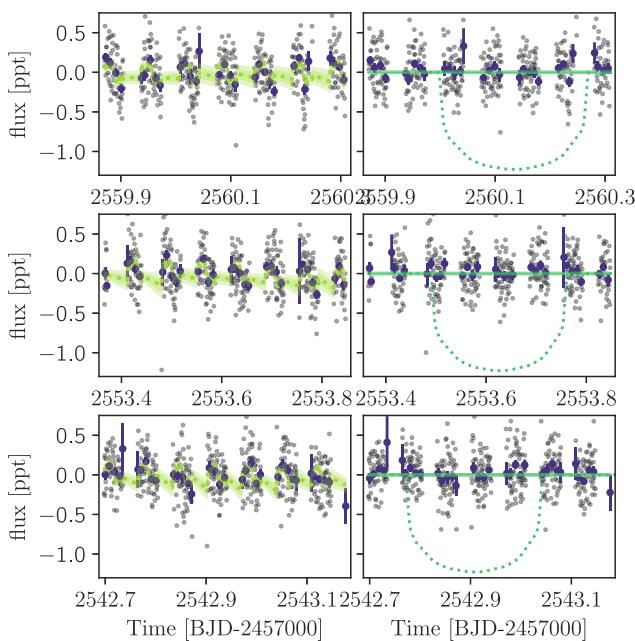
Figure 4. *CHEOPS* photometry for the three early and unsuccessful visits of HIP 9618. Left-hand plots show the raw PSF photometry, as well as best-fitting regions for a simple decorrelation model (green). The right-hand plots show the residual photometry, which together has an RMS of only 8 ppm h^{-1}. In both plots, 15-min flux bins are shown in purple. The expected transit model of HIP 9618 c is shown as a dashed line.

prove constraining on the orbit of HIP 9618 c, and will be published in a future analysis. This led us to schedule 9 aliases between 38 and 68 d on *CHEOPS*. Of these, three were priority 1 aliases, which had the highest chance of being observed – 40.2, 45.6, and 52.5 d aliases. The first was to verify if the system was near a 2:1 period ratio, the second was due to a marginal peak in the Keck/HIRES and Lick/APF RVs, and the third was due to this being close to the peak in our MonoTools solution.

After three unsuccessful observations (see Fig. 4), we successfully recovered a transit of HIP 9618,c with *CHEOPS* on the fourth attempt, shown in Fig. 5. As with previous cases (e.g. Osborn et al. 2022), this was close to the maximum suggested by MonoTools modelling, helping us to once again validate our modelling approach.

2.4 Spectra

2.4.1 FIES

We used the FIbre-fed Échelle Spectrograph (FIES; Frandsen & Lindberg 1999; Telting et al. 2014) mounted on the 2.56 m Nordic Optical Telescope (NOT) of Roque de los Muchachos Observatory (La Palma, Spain) to acquire 5 high-resolution ($R \sim 67\,000$) spectra of HIP 9618 over 15 d. We used 'Stellar parameter classification' (SPC; Buchhave et al. 2012, 2014) producing stellar parameters of $T_{\rm eff} = 5638 \pm 55$ K, $\log g = 4.44 \pm 0.10$, [m/H] $= -0.04 \pm 0.08$, $v\sin i = 2.2 \pm 0.5$ km s^{-1}, all of which are within the uncertainties of our final derived values presented in Section 3.1 and Table 3. The FIES RV measurements show no significant variation within the measurement uncertainties, however they remain too low-precision $\sigma_{\rm RV} > 150$ m s^{-1} to prove useful in detecting the reflex motion of the two planets.
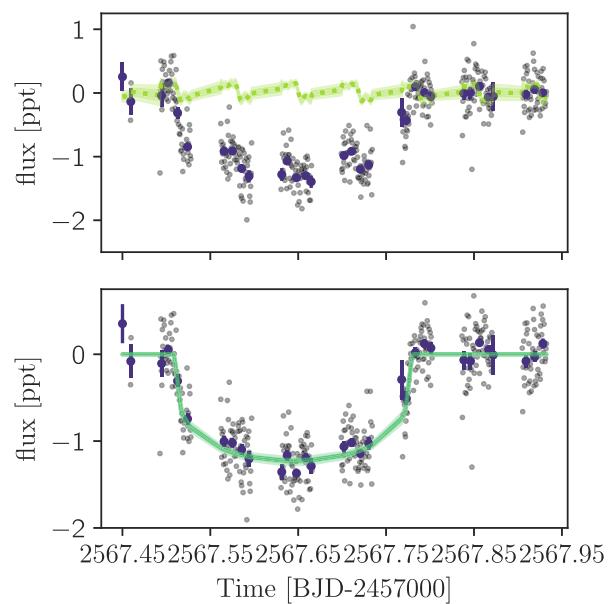

Figure 5. *CHEOPS* photometry of the visit at 52.5 d. *CHEOPS* data are represented by grey individual points and purple binned flux and errors. The upper figure shows the raw PIPE photometry with the detrending model 1 and 2σ error regions (in two transparency steps) and best-fitting (dashed line) in green. The lower figure shows detrending-removed *CHEOPS* photometry and 1 and 2σ error regions and best-fitting (dashed line) for the HIP 9618 c transit model in turquoise.

2.4.2 TRES

Four reconnaissance spectra were obtained between 2019 December and 2020 February using the Tillinghast Reflector Echelle Spectrograph (TRES; Fűrész 2008) mounted on the 1.5 m Tillinghast Reflector telescope at the Fred Lawrence Whipple Observatory (FLWO) atop Mount Hopkins, Arizona. TRES is a fibre-fed echelle spectrograph with a wavelength range of 390–910 nm and a resolving power of $R \sim 44\,000$. The spectra were extracted as described in Buchhave et al. (2010) and then used to derive stellar parameters using the Stellar Parameter Classification tool (SPC; Buchhave et al. 2012). SPC cross-correlates an observed spectrum against a grid of synthetic spectra derived from Kurucz atmospheric models (Kurucz 1992). The averaged stellar parameters ($T_{\rm eff} = 5637 \pm 50$ K, $\log g = 4.40 \pm 0.10$, [m/H] $= -0.08 \pm 0.08$, and $v\sin i = 2.5 \pm 0.5$ km s^{-1}) agree well with the adopted parameters.

2.4.3 HARPS-N

Between 2021 January 20 (UT) and 2022 January 30 (UT), we collected 13 spectra with the High Accuracy Radial velocity Planet Searcher for the Northern hemisphere (HARPS-N: $\lambda \in (378$–$691)$ nm, $R \approx 115\,000$; Cosentino et al. 2012) mounted at the 3.58-m Telescopio Nazionale Galileo (TNG) of Roque de los Muchachos Observatory in La Palma, Spain, under the observing programs ITP19_1 (see Table B1). The exposure time was set to 280–2400 s, based on weather conditions and scheduling constraints leading to a SNR per pixel of 28–107 at 550 nm. The spectra were extracted using the off-line version of the HARPS-N DRS pipeline (Cosentino et al. 2014), version HARPN_3.7. Absolute radial velocities (RVs) and spectral activity indicators (CCF_FWHM, CCF_CTR, BIS and Mont-Wilson S-index) were measured on the higher preicison *HARPS-N*

spectra using an on-line version of the DRS, the YABI tool[3], by cross-correlating the extracted spectra with a G2 mask (Baranne et al. 1996). We also used `serval` code (Zechmeister et al. 2018) to measure relative RVs by the template-matching, chromatic index (CRX), differential line width (dLW), and Hα, and sodium Na D1 & Na D2 indexes. The uncertainties of the relatives RVs measured with `serval` are in the range 0.7–3.1 m s^{-1}, with a mean value of 1.5 m s^{-1}. The uncertainties of absolute RVs measured with the online version of DRS (YABI) are in a the range 0.8–4.2 m s^{-1}, with a mean value of 1.6 m s^{-1}. Table B1 gives the time stamps of the spectra in BJD$_{TDB}$, `serval` relative RVs along with their 1σ error bars, and spectral activity indicators measured with YABI and `serval`. In the joint RV and transit analysis presented in Section 3.2 we used relative RVs measured from HARPS-N spectra with `serval` by the template-matching technique.

2.4.4 SOPHIE

SOPHIE is a stabilized échelle spectrograph dedicated to high-precision RV measurements on the 193-cm Telescope at the Observatoire de Haute-Provence, France (Perruchot et al. 2008). Before having been identified as TOI-1471, HIP 9618 was first observed in 2011 with *SOPHIE* as part of its volume-limited survey of giant extrasolar planets (e.g. Bouchy et al. 2009; Hébrard et al. 2016). After its identification as the host of the transiting planet candidate TOI-1471.01, it was re-observed in 2019–2021 with *SOPHIE* as part of its *TESS* follow-up. Overall, we secured 28 *SOPHIE* spectra of HIP 9618 in its high resolution mode (resolving power $R = 75\,000$). Depending on the weather conditions, their exposure times ranged from 3 to 20 min (typically 10 min) and their signal-to-noise ratio per pixel at 550 nm from 30 to 80. The corresponding radial velocities were extracted with the standard *SOPHIE* pipeline using cross correlation functions (Bouchy et al. 2009) and including CCD charge transfer inefficiency correction (Bouchy et al. 2013). Following the method described in Pollacco et al. (2008) and Hébrard et al. (2008), we estimated and corrected for the moonlight contamination using the second *SOPHIE* fibre aperture, which is targeted on the sky while the first aperture points towards the star. We estimated that only three spectra were significantly polluted by moonlight; one of them was too contaminated and was discarded, whereas the other two were corrected, with a correction value below 10 m s^{-1}.

Thus our final *SOPHIE* data set included 27 measurements showing uncertainties ranging from 1.6 to 3.9 m s^{-1} (see Table B2). The RVs show a 9-m s^{-1} dispersion around a blueshifting drift of about 200 m s^{-1} in 10 yr. The corresponding bisectors of the cross-correlation functions do not show any significant variation nor correlation with the RV, so there are no hints for RV variations induced by blend configurations nor stellar activity.

2.4.5 CAFE

Finally, we also observed TOI-1471 with the *CAFE* (Calar Alto Fiber-fed Echelle) spectrograph (Aceituno et al. 2013) mounted at the 2.2 m telescope of the Calar Alto observatory. A total of 22 spectra were obtained between 2019 December 18 and 2022 August 19 with typical signal-to-noise ratio of 30 (see Table B3). The data were reduced and the spectra extracted by using the observatory pipeline described in Lillo-Box et al. (2020), which also determines

[3]Available at http://ia2-harps.oats.inaf.it:8000.

Table 2. Key information for high-resolution Imaging.

Facility	Instrument	Filter	Image time [UT BJD]
Keck2	NIRC2	BrGamma	2020-05-28 2458997.82
SOAR	HRCam	I	2020-10-31 2459153.65
SAI-2.5m	Speckle Polarimeter	625nm	2020-12-03 2459186.25
Gemini	'Alopeke	562nm	2020-12-04 2459187.75
Gemini	'Alopeke	832nm	2020-12-04 2459187.75
Palomar	PHARO	BrGamma	2020-12-04 2459187.75
Gemini	'Alopeke	562nm	2021-10-17 2459504.8
Gemini	'Alopeke	832nm	2021-10-17 2459504.8

the radial velocity by performing cross-correlation against a solar binary mask. Usually, several spectra were obtained for each night. We binned the RVs per night. This implies a total of 10 measurements. We discarded the first one due to lack of radial velocity standards observed that night that prevented us from calculating and correcting for the relevant nightly zero point. Hence, nine measurements are available with a median uncertainty of 7 m s^{-1}.

2.5 High-resolution imaging

A detected exoplanet transit signal might be a false positive due to a background eclipsing binary or yield incorrect stellar and exoplanet parameters if a close companion exists and is unaccounted for (Furlan & Howell 2017, 2020). Additionally, the presence of a close companion star leads to the non-detection of small planets residing with the same exoplanetary system (Lester et al. 2021). Given that nearly one-half of FGK stars are in binary or multiple star systems (Matson et al. 2019), high-resolution imaging provides crucial information towards our understanding of exoplanetary formation, dynamics, and evolution (Howell et al. 2021).

As part of the standard process for validating *TESS* candidates (e.g. Ciardi et al. 2015), we observed HIP 9618 with a combination of high-resolution resources including near-infrared adaptive optics (AO) imaging at Palomar and Keck and optical speckle observations at Gemini-North, SOAR, and SAI-2.5m. While the optical observations tend to provide higher resolution, the NIR AO tend to provide better sensitivity, especially to lower mass stars. The combination of the observations in multiple filters enables better characterization for any companions that may be detected. *Gaia* DR3 is also used to provide additional constraints on the presence of undetected stellar companions as well as wide companions.

Detailed descriptions for the observations, reduction, and analysis for all five high-resolution instruments are found in Section A0.1, A0.2, A0.3, and A0.4 and summarized in Table 2. In summary, none of the observations revealed evidence for close-in ($\lesssim 1$ arcsec) stellar companions. However, the Palomar observations did detect a faint stellar companion 7 magnitudes fainter than the primary star and 3 arcsec to the south-west (PA = 235°). The companion star is Gaia DR3 94468978202368768.

2.6 Gaia and archival assessment

In addition to the high resolution imaging, we have used *Gaia* to identify any wide stellar companions that may be bound members of the system. Typically, these stars are already in the *TESS* Input Catalogue and their flux dilution to the transit has already been accounted for in the transit fits and associated derived parameters. There are no additional widely separated companions identified by *Gaia* that have the same distance and proper motion as HIP 9618 (see also Mugrauer & Michel 2020, 2021).

Table 3. Stellar information for HIP 9618. TIC v8 described by (Stassun et al. [2019]), Gaia DR3 by (Gaia Collaboration [2021]), Hipparcos by (Lindegren et al. [1997]). 2MASS by Cutri et al. ([2003]), and stellar parameters derived by our own analysis are described in Section [3.1].

Parameter	Value	Source
Name	HIP 9618	–
TOI	TOI-1471	–
TIC	306263608	TICv8
HD designation	HD 12572	–
Gaia DR3 ID	94468978202180352	Gaia DR3
RA [°, J2015.5]	30.904272	Gaia DR3
Dec [°, J2015.5]	21.280864	Gaia DR3
TESS mag	8.5725 ± 0.006	TICv8
G mag	9.02543 ± 0.00027	Gaia DR3
K mag	7.559 ± 0.021	2MASS
$T_{\rm eff}$ (K)	5609.0 ± 33.0	This work
R_s [$R_\odot$]	0.9662 ± 0.005	This work
M_s [$M_\odot$]	$1.022^{+0.043}_{-0.076}$	This work
$\log g$ (cgs)	$4.45^{+0.016}_{-0.033}$	This work

The faint stellar companion detected by Palomar was detected by *Gaia* (DR3 94468978202368768) but a full astrometric solution (parallax and proper motion) for this star is not yet available in DR3. However, the epoch of observations between *Gaia* (2016.0) and Palomar (2020.93) are sufficiently separate to use the proper motion as a test for boundedness. HIP 9618 has a proper motion of $\mu_\alpha = 158.8$ mas yr^{-1} and $\mu_\delta = 107.5$ mas yr^{-1}, which should produce an increase in separation of the two stars of $\Delta\alpha = 0.78$ arcsec and $\Delta\delta = 0.53$ arcsec for a total separation increase of 0.95 arcsec. The measured separation of the stars by *Gaia* (2016) is 2.1 arcsec and by Palomar (2020) is 3.1 arcsec – fully consistent with the measured proper motion of TOI 1471 and the companion star being a low-proper motion background star. Thus, the detected companion is almost certainly unbound and unrelated to the HIP 9618 system.

Additionally, the *Gaia* DR3 astrometry provides additional information on the possibility of inner companions that may have gone undetected by either *Gaia* or the high resolution imaging. The *Gaia* Renormalized Unit Weight Error (RUWE) is a metric, similar to a reduced chi-square, where values that are $\lesssim 1.4$ indicate that the *Gaia* astrometric solution is consistent with the star being single whereas RUWE values $\gtrsim 1.4$ may indicate an astrometric excess noise, possibly caused the presence of an unseen companion (e.g. Ziegler et al. [2020]). TOI 1471 has a *Gaia* DR3 RUWE value of 1.02 indicating that the astrometric fits are consistent with the single star model.

Due to the large proper motion of HIP 9618, we were also able to use archival photometric plates[4] to assess the possibility of a coincident bright background star. These observations provide a baseline of over 100 yr and therefore a relative offset of 25 arcsec, and find no sign of any bright source. POSS-I imaging from 1954 does detect the faint Gaia source (DR3 94468978202368768) 11 arcsec from HIP 9618, confirming that it is not a bound companion.

3 ANALYSIS

3.1 Stellar parameters

The stellar parameters for HIP 9618 are presented in Table [3]. The analysis of the co-added HARPS-N stellar spectrum has been carried

[4]Through the APPLAUSE project; https://www.plate-archive.org/query/

out by using the BACCHUS code (Masseron et al. [2016]) relying on the MARCS model atmospheres (Gustafsson et al. [2008]) and atomic and molecular line lists from Heiter et al. ([2021]). In brief, the surface gravity ($\log g = 4.47 \pm 0.10$) has been determined by requiring ionization balance of Fe I lines and Fe II line. A microturbulence velocity has also been derived (0.95 ± 0.1 km s^{-1}) by requiring no trend of Fe line abundances against their equivalent widths. The output metallicity ([Fe/H] $= -0.07 \pm 0.06$) is represented by the average abundance of the Fe I lines. An effective temperature of 5611 ± 31 K has been derived by requiring no trend of the Fe I lines abundances against their respective excitation potential.

We used the *HARPS-N* spectra to measure the stellar rotation ($v\sin i$) using the average of the Fe lines broadening after having subtracted the instrument and natural broadening. This technique led to an upper limit of the stellar rotation velocity of <3.5 km s^{-1}, which agrees well with the 2.5 ± 0.5 km s^{-1} derived from FIES spectra, both of which highlight a long stellar rotation period.

In a second step, we used the Bayesian tool PARAM (Rodrigues et al. [2014], [2017]) to derive the stellar mass, radius, and age utilizing the spectroscopic parameters and the updated *Gaia* luminosity along with our spectroscopic temperature. However, such Bayesian tools underestimate the error budget as they do not take into account the systematic errors between a set of isochrones to another due to the various underlying assumptions in the respective stellar evolutionary codes. In order to take into account those systematic errors, we combined the results of the two sets of isochrones provided by PARAM (i.e. MESA and Parsec) and add the difference between the two sets of results to the error budget provided by PARAM. We obtained a stellar radius and mass of respectively 0.97 ± 0.02 R$_\odot$ and 0.89 ± 0.07 M$_\odot$. Despite its nearly solar metallicity, the derived age from the isochrones indicates that the star is old (9 ± 4 Gyr). This is consistent with the fact that we do not detect any lithium in the atmosphere of the star, nor we detect a chromospheric activity in the core of the H & K Ca lines and that we find indications of a low rotation period.

However, we emphasize that although using two sets of isochrones may mitigate underlying systematic errors, our formal error budget for radius and luminosity may still be underestimated, as demonstrated by Tayar et al. ([2022]). For solar-type stars such as TOI-1471, absolute errors may rather be up to 4 per cent, 2 per cent, 5 per cent, and 20 per cent for, respectively radius, luminosity, mass, and age.

3.1.1 Rotation

Based on Noyes et al. ([1984]) and Mamajek & Hillenbrand ([2008]) activity–rotation relations and using ($B-V$) of 0.688 and the $\log R'_{\rm HK}$ measured with YABI (-4.972 ± 0.044), we estimated a rotation period of HIP 9618 of 29.0 ± 5.9 d and 30.4 ± 3.5 d, respectively. This is consistent with the $v\sin i$ upper limits derived from spectra. Using the activity–age relation of Mamajek & Hillenbrand ([2008]) we also found an age of HIP 9618 to be in a range of 3.6–7.3 Gyr, consistently with the age determined with the isochrones within the errorbars.

3.1.2 Radius

We employed a Markov–Chain Monte Carlo (MCMC) modified infrared flux method (IRFM; Blackwell & Shallis [1977]; Schanche et al. [2020]) to determine the radius of HIP 9618 by computing the stellar bolometric flux and obtaining the effective temperature and angular diameter. This was done by fitting spectral energy distributions

(SEDs), constructed using priors from our spectral analysis, to broadband fluxes and uncertainties from the most recent data releases for the following bandpasses; *Gaia* G, G$_{BP}$, and G$_{RP}$, 2MASS J, H, and K, and *WISE* W1 and W2 (Skrutskie et al. 2006; Wright et al. 2010; Gaia Collaboration 2021). The angular diameter is converted to a radius using the offset-corrected *Gaia* parallax (Lindegren et al. 2021). To account for stellar model biases we conducted a Bayesian modelling averaging of the ATLAS (Kurucz 1993; Castelli & Kurucz 2003) and PHOENIX (Allard 2014) catalogues to produce weighted averaged posterior distribution of the stellar radius and obtain a value of $R_s = 0.962 \pm 0.008 \, R_\odot$. Due to the non-luminous and faint nature of the companion we do not include a second SED and corresponding free parameters in the MCMC.

3.2 Combined photometry and RV model

Once we had successfully recovered the true period of HIP 9618 c we investigated the properties of the two transiting planets by modelling both the radial velocities and the *TESS* and *CHEOPS* photometry together. The model was built in PyMC3 (Salvatier et al. 2016) using the Keplerian orbits and transit models of exoplanet (Foreman-Mackey et al. 2021). For the stellar parameters, we use the values derived in Section 3.1 as priors to our analysis (see Table 3). The SNR and the partial nature of the two ground-based transit observations with LCO (see Section 2.2) meant we did not include them in the combined model.

HIP 9618 appears to be a quiet old G star without evidence of stellar activity in the *TESS* light curve, and thanks to the quaternion detrending systematic noise appears minimal. Therefore we chose to remove long-duration trends using a basis spline with a knot length of 1.25 d. To avoid influencing the spline fit, the six transits were masked using the initially derived ephemerides. To speed up the modelling, we then kept only 4.5 transit durations of photometry around mid-transit. A log jitter term was included to incorporate systematic errors not incorporated into the *TESS* flux errors.

For the *CHEOPS* data, we performed simultaneous linear decorrelation with three normalized vectors from the *CHEOPS* metadata – two incorporating roll angle (Φ) trends ($\sin \Phi$ & $\cos \Phi$) and one for background flux. We also included a log jitter term to account for excess systematic noise. In order to remove shorter time-scale flux variation as a function of roll angle, we included a common cubic bspline with breakpoints every ~8 degrees. The decorrelation terms and spline model were shared across all four *CHEOPS* visits.

In Section 4.1, we explore the possible characteristics of a massive companion in the system. This gives the possibility of an M-dwarf companion to HIP 9618 which could provide unaccounted dilution (and also depth difference between *TESS* and *CHEOPS* photometry). We therefore include two dilution terms in our combined analysis using the derived expected magnitude difference of the companion in *R* & *I* band (interpolated from primary and secondary masses) to represent dilution in *CHEOPS* and *TESS* bands respectively (9.0 ± 2.1 & 7.4 ± 1.8).

We use informative priors on limb darkening parameters for both *TESS* and *CHEOPS* passbands, using the theoretical quadratic limb darkening parameters of Claret (2018, 2021). To account for systematic errors, we inflate the uncertainties to 0.05 in all cases.

For the radial velocity modelling, we include a relative offset for each instrument, with priors set from the average and standard deviation of the points. We also included a jitter term with a broad lognormal prior. A quadratic polynomial was used to model the large observed drift, with normal priors with $\mu = 0.0$ and $\sigma = 0.05$ and 0.005 for linear and quadratic terms. Inspection of the activity indices

from *HARPS-N*, *SOPHIE*, and *CAFE* reveals no clear rotation signal and no correlation with the radial velocities, which is consistent with the lack of obvious variability seen in the photometry. Therefore we chose not to model activity using e.g. Gaussian Processes, and instead use only the planets Keplerian orbits.

We modelled radius ratio, R_p/R_s, using a broad lognormal prior to avoid unphysical negative values. We tested fitting RV semi-amplitude, K_{pl}, using both broad lognormal and a free uniform prior (allowing negative values), both of which converged to consistent solutions. We tested modelling both with and without eccentricity, testing both the Van Eylen et al. (2019) multiplanet prior and the general Kipping (2013) priors which gave consistent results. We use the uniform K_{pl} prior and Kipping (2013) eccentricity priors as the final model here.

The results of our combined model can be seen in Figs 5, 6 and 7, while the derived planetary properties can be found in Table 4. All priors and posteriors for the combined modelling are shown in Table C1

4 DISCUSSION

4.1 RV drift

We measure a sizable RV drift of $-19.2 \, \mathrm{m \, s^{-1}}$ per year (see Fig. 7). Comparisons of combined models with linear and quadratic RV trends also shows that the RV drift prefers a model with curvature ($-0.7 \pm 0.05 \, \mathrm{m \, s^{-1} yr^{-2}}$). This is therefore likely indicative of a massive outer companion in the system. Acceleration between Hipparcos and Gaia astrometric measurements is a key technique to characterizing such outer companions. However, the HGAS catalogue contains only a very minimal deviation from a linear ephemeris (2.647 chi-square difference). *Gaia* DR3 does not flag HIP 9618 as a 'non_single_star', though it does find a 6-sigma excess astrometric noise, however this corresponds to a dispersion of only 80 µas, and as discussed in Section 2.6 and, as discussed in Section 2.6, to a RUWE of 1.03 very likely suggests a single star.

In order to characterize the undetected outer candidate, we used the orvara package (Brandt et al. 2021) to model the RV drift and the Hipparcos & Gaia astrometric data jointly. Orvara accessed the Hipparcos and *Gaia* astrometry (which reveal no significant acceleration despite a 20-yr baseline), and we also included our RVs with the best-fitting models for planets b & c, and the best-fitting RV offsets for each instrument removed from the data. Using our derived stellar mass as a prior, we ran 100 walkers for chains of 25 000 steps. The result, after pruning the burn-in, is a distribution of 40 000 independent samples which are consistent with the observed RV and astrometric data.

However, we also have information derived from our high-resolution imaging observations, which are able to rule out close bright companions to HIP 9618. In order to use this information, we modified orvara to compute the companion separation at each imaging epoch. We used a combination of the main sequence models of Pecaut & Mamajek (2013)[5] and the Brown Dwarf models of Baraffe et al. (2003) to translate from companion masses derived by orvara into magnitudes. We either interpolate these to the observed bands or use the closest available magnitude depending on the filter.

Given the implied separation and ΔMag, as well as an extra factor of 0.25 mag to account for systematic noise, we were then able to

---

[5] http://www.pas.rochester.edu/~emamajek/EEM_dwarf_UBVIJHK_colors_Teff.txt
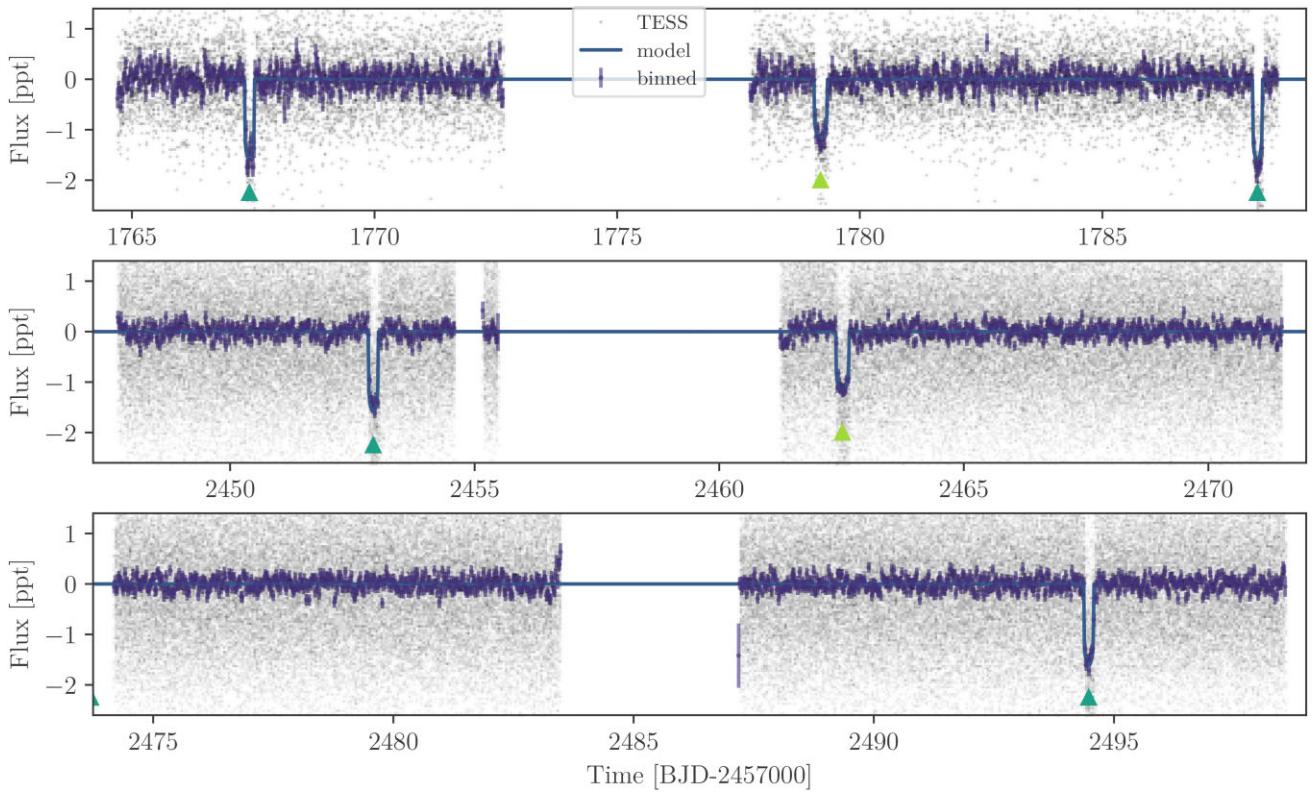
Figure 6. *TESS* photometry of HIP 9618 showing the four transits of HIP 9618 b and two transits of HIP 9618 c. Individual points are plotted as grey dots, purple circles show binned flux and errors, and the blue line corresponds the best-fitting transit model.
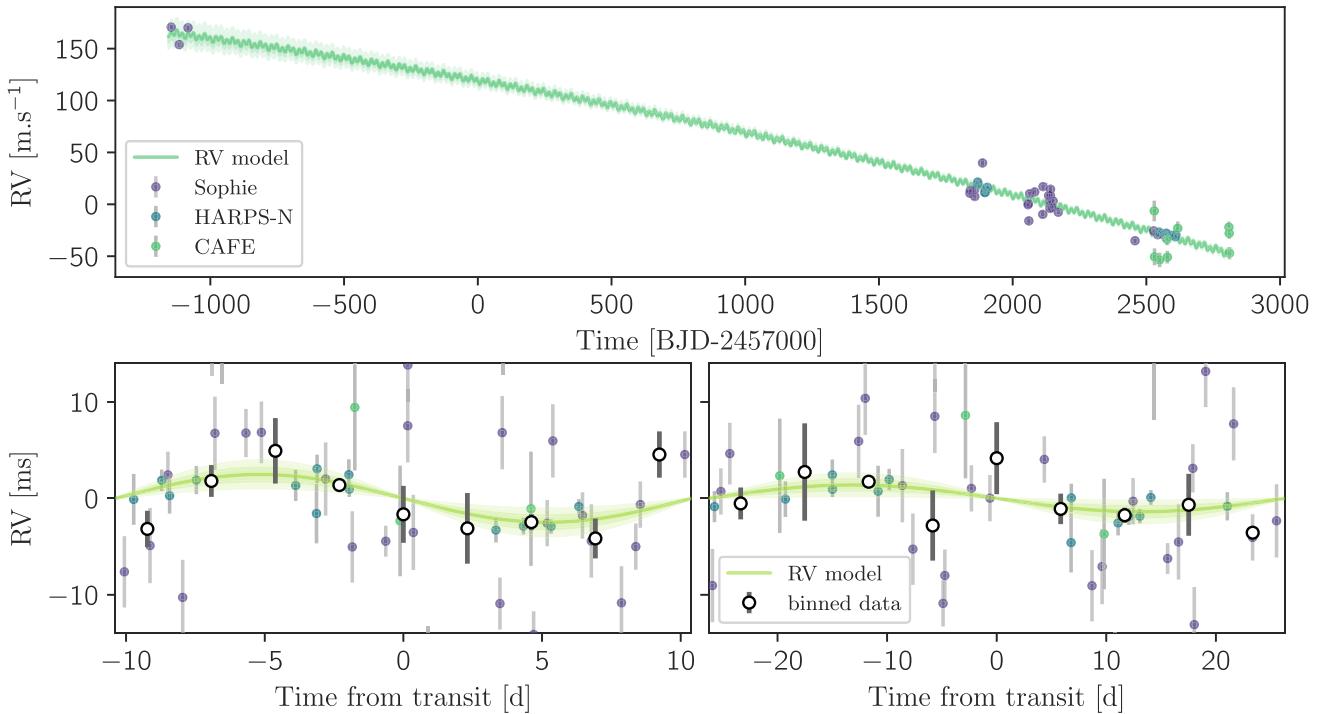

Figure 7. *SOPHIE*, *CAFE*, and *HARPS-N* radial velocities for HIP 9618. Upper: RVs adjusted for intraspectrograph offsets, and the linear polynomial model for RV drift. Lower panels: RVs with offsets and trend removed showing the reflex motion from HIP 9618 b (left-hand panel) and c (right-hand panel). Filled areas represent 1 and 2σ regions in two transparency steps. White points with black borders represent phase-binned RVs.

Table 4. Derived planetary parameters. * refers to 3-sigma upper limit (and other limits derived using this value).

Parameter	HIP 9618 b	HIP 9618 c
Epoch, t_0 [BJD-2457000]	1767.42089 ± 0.00057	1779.1919 ± 0.001
Period, P (d)	$20.772907 \pm 2.3e - 05$	$52.563491 \pm 7.2e - 05$
Semi-major axis, a (au)	$0.1438^{+0.0025}_{-0.0037}$	$0.2669^{+0.0046}_{-0.0069}$
Radius ratio, R_p/R_s	0.03699 ± 0.00037	0.03171 ± 0.00034
Duration, t_D (d)	$0.2047^{+0.0015}_{-0.0014}$	0.2731 ± 0.0012
Radius, R_p [$R_\oplus$]	3.9 ± 0.044	3.343 ± 0.039
Insolation, I_p (Wm^{-2})	54900^{+3100}_{-2100}	15930^{+890}_{-600}
Surface Temp., T_{eq} (K)	$663.4^{+9.1}_{-6.3}$	$486.9^{+6.6}_{-4.6}$
RV Semi-amplitude, K (m s^{-1})	2.48 ± 0.71	1.39 ± 0.58
Mass, $M_p/M_\oplus$ [$M_\oplus$]	10.0 ± 3.1	$<<18.3 \pm 1.7$
Eccentricity, e	$0.22^{+0.25}_{-0.15}$	$0.23^{+0.25}_{-0.16}$
Arg. of Periasteron, ω	0.1 ± 2.2	-0.1 ± 2.1
TSM	$166.0^{+74.0}_{-40.0}$	>42.0
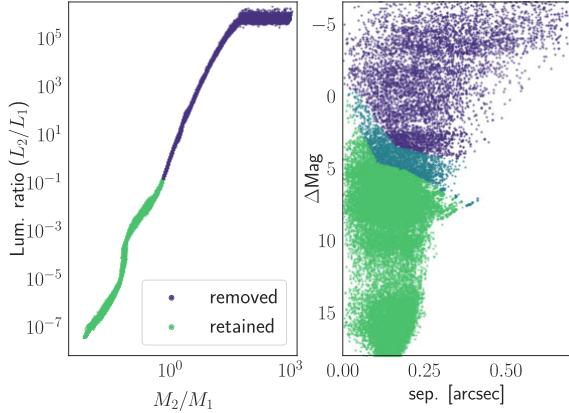
Figure 8. Samples generated with `orvara` which were accepted (in green) or rejected (in dark blue) due to a luminosity and therefore relative flux incompatible with the stacked spectrum (left-hand panel), or due to a magnitude difference (or Δmag) incompatible with the multiple high-resolution images obtained in follow-up photometry. Although this pruning was performed on a per-magnitude basis, this plot shows the average magnitude across all useful bands, with samples removed due to only some imaging observations shown in blue.

Figure 9. Kernel density function showing the distribution of semimajor axis and mass ratio for long-period companions compatible with all available observable data.

compute whether our imaging observations would have detected the companion created by `orvara`. We also have radial velocity observations and stacked spectra which should be able to resolve close-in bright binary companions. Assuming a conservative detectable flux ratio of 15 per cent (equivalent to a K5 star), we also removed samples which would have been detectable as contamination in e.g. the CCF. Finally, given the inner two planets appear to be a typical multiplanet system, it is very unlikely that the low-mass companion would have extremely close encounters with the inner reaches of this system. Therefore we also included a threshold on the perihelion distance of 0.78 au – three times the orbital distance of HIP 9618c. This resulted in removing ~ 53 per cent of the samples generated by `orvara` – mostly those from high-mass, large-separation, and high-eccentricity regimes (see Fig. 8).

The remaining samples (shown in Fig. 9) therefore represent those which are consistent with the RV trend, (lack of) astrometric acceleration, imaging constraints, the lack of extra lines in the combined spectrum, and the assumed stability of the internal multiplanet system. The companion is therefore likely a brown dwarf or low-

mass M dwarf close to the hydrogen burning limit with a mass of $0.08^{+0.12}_{-0.05}M_\odot$ and a semimajor axis of $26.0^{+19.0}_{-11.0}$ au.

Our analysis of the orbit of HIP 9618 B hints that the outer companion (inclination $89° \pm 6°$) is closely aligned with the transiting planets (average inclination of 89.77 ± 0.12). This tightly constrained inclination is due to two factors. First the astrometric shift between Hipparcos and *Gaia* appears to be linear rather than the 2D shift expected from a face-on orbit. Secondary the model tries to maximize the RV trend – which is substantial – while minimizing the secondary mass – which is limited by the strict upper mass limits from the non-detection in high-constrast imaging and the astrometric amplitude. This is consistent with observations of small planet transiting systems which are far more likely to host aligned binary companions than the stellar average (Christian et al. 2022).

This approach also allows us to assess the detectability of the companion. In the Ks band, the magnitude difference to the primary star is expected to be only $6.8^{+1.2}_{-2.2}$, however we estimate it is currently at a separation of only 0.143 ± 0.05 arcsec, which may make imaging the companion challenging.

This analysis also rests on the assumption that the observed RV variation is exclusively from a single external companion. If, for example, a giant planet and low-mass star both exist on long

Table 5. Posterior distributions of the internal structure parameters of HIP 9618 b and c. The values correspond to the median and the 5 and 95 percentile of the distributions.

Internal structure parameter	HIP 9618 b	HIP 9618 c
M_{core}/M_{total}	$0.13^{+0.13}_{-0.12}$	$0.13^{+0.13}_{-0.11}$
M_{water}/M_{total}	$0.23^{+0.24}_{-0.21}$	$0.23^{+0.24}_{-0.21}$
$\log M_{gas}$ [$M_\oplus$]	$-0.15^{+0.19}_{-0.23}$	$-0.59^{+0.27}_{-0.47}$
Fe_{core}	$0.90^{+0.09}_{-0.08}$	$0.90^{+0.09}_{-0.08}$
Si_{mantle}	$0.40^{+0.08}_{-0.05}$	$0.40^{+0.08}_{-0.05}$
Mg_{mantle}	$0.45^{+0.11}_{-0.11}$	$0.45^{+0.11}_{-0.11}$

orbits in this system, then this could also produce the observed RV curvature. Hence, monitoring of HIP 9618 over a series of years with high precision spectrographs is needed to confirm the hypothesis presented here.

4.2 Interior composition

Given we have both mass and radius values for HIP 9618 b and c, we are able to constrain their mean densities. This allows us to model the internal structure of the planets. We use the method described in Leleu et al. (2021), which is based on Dorn et al. (2017). We will only outline the most important aspects of the Bayesian inference model here, namely the observational input parameters, the priors, and the main assumptions that are part of the forward model used to calculate the likelihood of the sampled internal structure parameters.

We assume planets that are spherically symmetric with four fully distinct layers: An inner iron core, a silicate mantle, a water layer, and a pure H/He atmosphere. Our forward model uses equations of state from Hakim et al. et al. (2018), Sotin et al. (2007), Haldemann et al. (2020), and Lopez & Fortney (2014) to model these layers. Moreover, the current version of our model makes two important assumptions: First, we assume a fixed temperature and pressure at the atmosphere–water boundary and model the gas layer separately from the rest of the planet, which means we neglect any influence of the gas layer on the solid part. Secondly, we follow Thiabaud et al. (2015) and assume that the Si/Mg/Fe ratios of the planets match the ones of the star exactly. Furthermore, we model both planets in the system simultaneously. In a future version of our model, we plan implementing more recent results from Adibekyan et al. (2021), which shows that while the composition of the star and its planets correlate, they do not necessarily share identical composition.

The model takes as input parameters various planetary and stellar observables, more specifically the transit depths, relative masses and periods of the planets and the mass, radius, age, effective temperature, metallicity, and Si and Mg abundances of the star. We assume a prior that is uniform in log for the gas mass fraction. The prior we assume for the layer mass fractions of the iron core, silicate mantle, and the water layer (with respect to the solid planet) is uniform, with the added conditions that they need to add up to 1 and the water mass fraction has a maximum value of 0.5 (Thiabaud et al. 2014). We stress that the results of our model depend to a certain extent on the chosen priors and repeating the calculation with very different priors might lead to different posterior distributions for the internal structure parameters.

The results of our model for both planets are summarized in Table 5. The full corner plots is shown in Fig. D1. For both HIP 9618 b and c, the posterior of the water mass fraction is almost completely unconstrained. Conversely, the posteriors of the gas masses are reasonably well constrained, considering the rather high uncertainty on the mass of planet c. For planet b, the posterior distribution of the gas mass has a median of $0.71^{+0.40}_{-0.29} M_\oplus$ (error bars are the 5 and 95 percentile of the posterior), corresponding to a thickness of $1.76^{+0.26}_{-0.27} R_\oplus$ of the gas layer. For planet c, the median of the gas mass is $0.26^{+0.22}_{-0.17} M_\oplus$, with a thickness of $1.47^{+0.40}_{-0.32} R_\oplus$ of the gas layer.

4.3 Planet c

HIP 9618 c was re-detected at a 52.5 d period with extremely high confidence in our *CHEOPS* data. We find a transit depth of 1.2 ppt which, given the magnitudes of all known nearby stars, cannot be due to a blend. As discussed in Section 4.1, all available data suggests the bound stellar (or brown dwarf) companion in the system is low-mass and extremely unlikely to be the source of any signal. The nearby background stellar contaminant discussed in Section 2.6 is also not bright enough to cause the observed transits of planet c.

We clearly see the reflex motion of planet b in our radial velocities, confirming it as a true planet orbiting HIP 9618. Thanks to their low mutual inclinations and stability, multiplanet systems have extremely low false positive rates (Lissauer et al. 2012). We also find, thanks to precise stellar parameters and high-SNR transit observations, that the transit duration matches extremely closely to that from our derived stellar density, implying both that planet c transits our proposed target star, and that its orbit is likely close to circular. Given all of these considerations, we are therefore confident in calling both HIP 9618 b & c bona fide planets.

Despite a mass measurement for HIP 9618 b we only find a marginal detection of the reflex motion of HIP 9618 c in the RVs. Indeed, our combined model finds a semi-amplitude of only $1.39 \pm 0.58\,\mathrm{m\,s^{-1}}$ and a 3σ mass limit of $<18\,M_\oplus$. With a far longer period this could simply be due to the reduction in semi-amplitude with orbital period ($K_p \propto P^{-1/3}$). However, it appears more likely (~ 66 per cent according to our combined model) that the mass of HIP 9618 c is lower than that of HIP 9618 b. We also found eccentricities for the two planets consistent with zero (at $<2\sigma$).

Interestingly, we found HIP 9618 c to be orbiting just beyond a 5/2 integer ratio (2.530). Although this is a third order resonance, there is still the possibility that TTVs may be present. However, when modelling the system using floating individual transit times for each of the four transits of HIP 9618 b and three transits of HIP 9618 c and found no obvious TTVs despite timing constrained to <5 min.

4.4 Similar systems

Three other bright ($G < 10$) host stars host a system of multiple Neptune-like transiting planets ($3 < R_p < 5 R_\oplus$). TOI-2076 hosts planets at 3.5 and $3.2 R_\oplus$ on orbits of 21 and 35 d, respectively (Osborn et al. 2022). HD 28109 hosts planets with 4.2 and 3.25 $R_\oplus$ on orbits of 56 and 84 d (Dransfield et al. 2022). HD 191939 hosts three such planets with radii of 3.4, 3.1, and $3.0 R_\oplus$ on orbits of 9, 29, and 38 d (Badenas-Agusti et al. 2020). In all of these cases, HIP 9618 included, it appears that these planet's ability to maintain thick atmospheres is likely helped by their longer orbital periods and therefore low insolation. This is partly because, at longer periods and lower insolations, the typical upper radius limit is not sculpted by the 'hot Neptune desert' – a regime where high evaporation causes atmospheric loss.

These planets, all found by *TESS*, are bright enough to allow precise radial velocities, and therefore we have masses for the planets and constraints on the outer companions. In the majority of these cases, the inner Neptune is the most massive despite not frequently
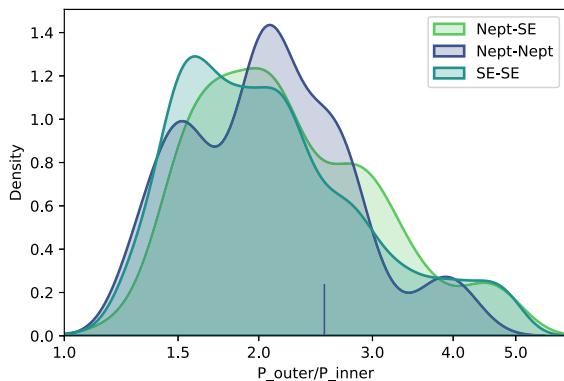
Figure 10. Period ratios for neighbouring planets in multisystems split into three groups – Neptune pairs ($3 < R_p < 5R_\oplus$), super-earth pairs ($R_p < 3R_\oplus$), and dissimilar pairs spanning the two. Exoplanets come from the NASA exoplanet archive (Akeson et al. 2013). Ratio populations are displayed using a kernel density estimator (KDE; Sheather & Jones 1991; Waskom 2021). The dash at the bottom shows the position of HIP 9618.

holding the largest radius. Radial velocity measurements also revealed that HD 139139 also hosts a high-mass outer companion on a long-period orbit (Lubin et al. 2022; Orell-Miquel et al. 2023), much like HIP 9618. Whether such companions could have helped produce their similar architectures is an open question.

To put HIP 9618 into context, we also studied the period ratios of neighbouring pairs in transiting multiplanet systems. HIP 9618 is unusual in that it hosts two planets larger than the typical radius for multiplanet systems – both are closer to Neptune in radius than to typical super-Earths ($\sim 1.5R_\oplus$) or even mini-Neptunes ($\sim 2.2R_\oplus$). We find that, while all small planets typically have period ratios peaking at ~ 2, Neptune–Neptune pairs (defined here as planets with $3 < R_p < 5R_\oplus$) have significantly larger average period ratios than both pairs of small planets ($<3R_\oplus$) and dissimilar pairs (Fig. 10). This effect is even stronger when divided by mass rather than radius, however the fact that small planets are dominated by TTV masses and therefore period ratios close to e.g. 1.5 may bias this data set. Hence, their larger-than-average planetary sizes may explain why the HIP 9618 planetary system did not end up in (or did not persist as) a closely orbiting resonant chain, unlike many multisystems of smaller planets.

4.5 Characterization potential

With its bright IR magnitude ($K = 7.8$), the HIP 9618 system is amenable to atmospheric follow-up. We calculate Transmission Spectroscopy Metric (TSM; Kempton et al. 2018) values of $166.0^{+74.0}_{-40.0}$ for HIP 9618 b using our derived mass and radius, and >42.0 for HIP 9618 c.

Nevertheless, these two planets are some of the most amenable sub-Neptunes on long orbits around solar-like stars (see Fig. 11). To test the observability of spectral features with *JWST* we used the PANDEXO package (Batalha et al. 2017) to produce simulated spectra of the two planets from a single transit. We chose to test the NIRSpec/BOTS/G395M which is optimal for this target both because saturation is avoided at the redder modes and because the information content is highest in this mode for sub-Neptunes (Guzmán-Mesa et al. 2020). We used our derived planetary parameters as inputs, using the 2-sigma upper limit mass for HIP 9618 c. As model spectra we used cloudy and clear equilibrium chemistry models from Fortney et al. (2010) at 750 & 500K for HIP 9618 b & HIP 9618 c, respectively.
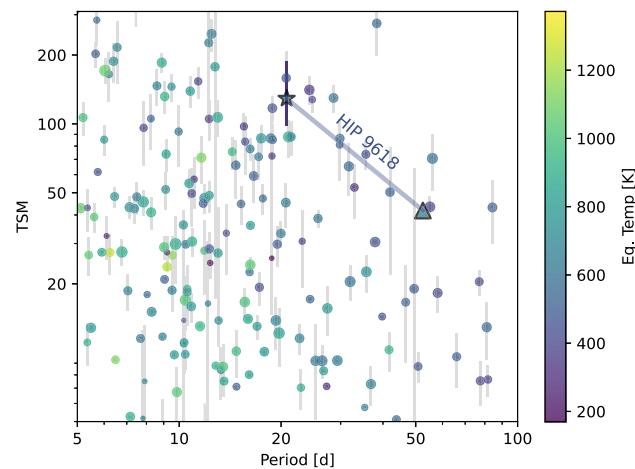
Figure 11. Transmission spectroscopy metrics (TSMs) and uncertainties for small ($R_p < 5R_\oplus$) exoplanets as a function of orbital period and equilibrium temperature. Exoplanetary data is taken from the NASA Exoplanet Archive (Akeson et al. 2013). HIP 9618 b is shown as a star and the 3-sigma lower limit is shown for HIP 9618 c as a triangle.
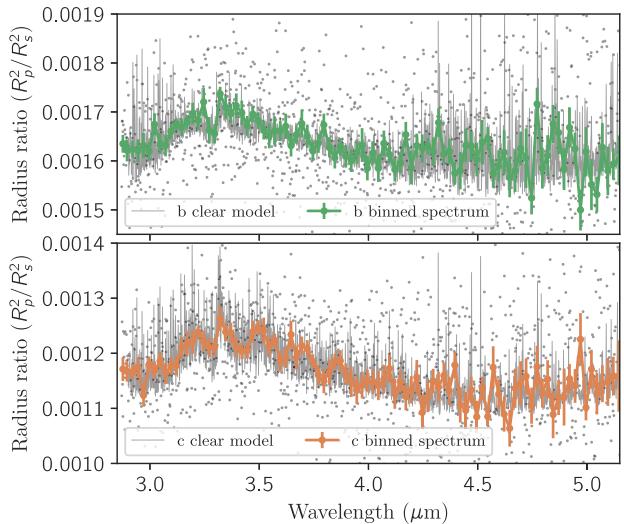
Figure 12. Simulated *JWST* spectra of HIP 9618 b (upper panel) and c (lower panel) using PANDEXO for a clear atmospheric model. Small dark points are individual *JWST* simulated high-resolution data, while coloured tickmarks represent the spectra sampled in 25 nm bins. Lines represent the input models from Fortney et al. (2010).

Simulated outputs can be seen in Fig. 12, where we find spectral features including the CH_4 feature at 3.3 µm clearly visible in both planets in both cloudless and moderately cloudy models (not shown).

5 CONCLUSIONS

TESS has proved exceptional for finding transiting planets around bright stars which are amenable to follow-up including high-resolution spectroscopy and transmission spectroscopy. HIP 9618 b, found by *TESS* to have a period of $20.772907 \pm 2.3e - 05$ d and a radius of $3.9 \pm 0.044\,R_\oplus$ is an excellent example of this. The parent star, an old (9 ± 4 Gyr) sunlike ($T_{\rm eff} = 5611 \pm 31$) star, has bright visual and infrared magnitudes ($G = 9.03$, $K = 7.56$) that helped enable precise follow-up RVs which found it to have a mass of

$10.0 \pm 3.1\,M_\oplus$. The precise radius and mass enable internal structure modelling which suggest the planet to have a 6.8 ± 1.4 per cent Hydrogen–Helium gaseous envelope and potentially a water-rich core. With a TSM of 103 ± 18, it is one of the few highly-rated warm ($T_{\rm eq} < 750$ K small planets orbiting a solar-like star. Simulations using PANDEXO suggest spectral features could be readily detectable in its atmosphere with a single *JWST* transit observation.

Unlike HIP 9618 b, *TESS* was unable to adequately detect HIP 9618 c at the true period. This is because, for planets on long periods not at the ecliptic poles, *TESS*'s short observation windows (27 and 54 d in the case of HIP 9618) do not enable it to observe consecutive transits. In the case of HIP 9618 c, *TESS* saw two transits spaced by 680 d – a 'Duotransit' candidate with a radius of $3.343 \pm 0.039\,R_\oplus$. We modelled the two transits using MonoTools and used *CHEOPS* to search the highest probability period aliases, successfully recovering a transit on the fourth observation and finding a period of 52.56349 d. Our RVs do not find a reliable mass for HIP 9618 c, but we can place a 3σ upper limit of $< 18 M_\oplus$. This suggests that planet c is less massive than b. Establishing a true mass may be possible with future RV measurements, which would in turn be key to enable accurate atmospheric characterization. Even using a conservative upper mass limit, it is likely that HIP 9618 c becomes one of the few characterizable planets orbiting a Sun-like star with an equilibrium temperature below 500 K.

Due to its bright magnitude, archival RV measurements exist for HIP 9618 taken with the *SOPHIE* spectrograph starting 8 yr before the detection of the candidate planets. This displays a clear ~ 200 m s^{-1} long-term trend consistent with a massive outer companion. Combined with the 20-yr baseline of *Hipparcos* and *Gaia* astrometric measurements, and high-resolution imaging follow-up observations, we are able to constrain the mass and orbit of this outer companion, finding that a companion near the hydrogen burning limit orbiting at 15–50 au best fits the observations. This companion can be better constrained with long-term RV monitoring, data from the *Gaia* extended mission, and potentially even with targeted direct imaging in the IR (e.g. Bonavita et al. 2022).

This detection makes HIP 9618 one of only five bright ($K < 8$) transiting multiplanet systems which hosts a planet with $P > 50$ d, opening the door for atmospheric characterization of a regime of warm ($T_{\rm eq} < 750$ K) sub-Neptunes.

DATA AVAILABILITY

The *TESS* data presented here is publicly accessible at MAST at http://mast.stsci.edu. All CHEOPS data presented here will be uploaded to CDS on publication of this paper https://cdsarc.cds.unistra.fr/viz-bin/cat/J/MNRAS/523/3069. Radial velocities are included in the tables found in the appendix. Ground-based photometry and imaging is publicly available through ExoFOP at https://exofop.ipac.caltech.edu/tess/

REFERENCES

Aceituno J. et al., 2013, A&A, 552, A31
Adibekyan V. et al., 2021, Science, 374, 330
Akeson R. L. et al., 2013, PASP, 125, 989
Allard F., 2014, in Booth M., Matthews B. C., Graham J. R., eds, Proc. IAU Symp. 299, Exploring the Formation and Evolution of Planetary Systems. Cambridge Univ. Press, Cambridge, p. 271

Badenas-Agusti M. et al., 2020, AJ, 160, 113
Baraffe I., Chabrier G., Barman T. S., Allard F., Hauschildt P. H., 2003, A&A, 402, 701
Baranne A. et al., 1996, A&AS, 119, 373
Batalha N. E. et al., 2017, PASP, 129, 064501
Benz W. et al., 2021, Exp. Astron., 51, 109
Blackwell D. E., Shallis M. J., 1977, MNRAS, 180, 177
Bonavita M. et al., 2022, MNRAS, 513, 5588
Bouchy F. et al., 2009, A&A, 505, 853
Bouchy F., Díaz R. F., Hébrard G., Arnold L., Boisse I., Delfosse X., Perruchot S., Santerne A., 2013, A&A, 549, A49
Brandt T. D., Dupuy T. J., Li Y., Brandt G. M., Zeng Y., Michalik D., Bardalez Gagliuffi D. C., Raposo-Pulido V., 2021, AJ, 162, 186
Brown T. M. et al., 2013, PASP, 125, 1031
Buchhave L. A. et al., 2010, ApJ, 720, 1118
Buchhave L. A. et al., 2012, Nature, 486, 375
Buchhave L. A. et al., 2014, Nature, 509, 593
Castelli F., Kurucz R. L., 2003, in Piskunov N., Weiss W. W., Gray D. F., eds, Proc. IAU Symp. 210, Modelling of Stellar Atmospheres. Cambridge Univ. Press, Cambridge, p. A20
Christian S. et al., 2022, AJ, 163, 207
Ciardi D. R., Beichman C. A., Horch E. P., Howell S. B., 2015, ApJ, 805, 16
Claret A., 2018, A&A, 618, A20
Claret A., 2021, Res. Notes Am. Astron. Soc., 5, 13
Collins K. A., Kielkopf J. F., Stassun K. G., Hessman F. V., 2017, AJ, 153, 77
Cosentino R. et al., 2012, in McLean I. S., Ramsay S. K., Takami H., eds, Proc. SPIE Conf. Ser. Vol. 8446, Ground-based and Airborne Instrumentation for Astronomy IV. SPIE, Bellingham, p. 84461V
Cosentino R. et al., 2014, in Ramsay S. K., McLean I. S., Takami H., eds, Proc. SPIE Conf. Ser. Vol. 9147, Ground-based and Airborne Instrumentation for Astronomy V. SPIE, Bellingham, p. 91478C
Cutri R. M. et al., 2003, 2MASS All Sky Catalog of point sources. Available at: http://irsa.ipac.caltech.edu/applications/Gator/
Dekany R. et al., 2013, ApJ, 776, 130
Dobos V., Charnoz S., Pál A., Roque-Bernard A., Szabó G. M., 2021, PASP, 133, 094401
Dorn C., Venturini J., Khan A., Heng K., Alibert Y., Helled R., Rivoldini A., Benz W., 2017, A&A, 597, A37
Dransfield G. et al., 2022, MNRAS, 515, 1328
Espinoza N., 2018, Res. Notes Am. Astron. Soc., 2, 209
Foreman-Mackey D. et al. 2021, J. Open Source Softw., 6, 3285
Fortney J. J., Shabram M., Showman A. P., Lian Y., Freedman R. S., Marley M. S., Lewis N. K., 2010, ApJ, 709, 1396
Frandsen S., Lindberg B., 1999, in Karttunen H., Piirola V., eds, The Third MONS Workshop: Science Preparation and Target Selection, Astrophysics with the NOT. Aarhus Universitet, Aarhus, Denmark, p. 71
Fűrész G., 2008, PhD thesis, University of Szeged, Hungary
Furlan E., Howell S. B., 2017, AJ, 154, 66
Furlan E., Howell S. B., 2020, ApJ, 898, 47
Furlan E. et al., 2017, AJ, 153, 71
Gaia Collaboration 2021, A&A, 649, A1
Garai Z. et al., 2023, A&A, 674, A44
Guerrero N. M. et al., 2021, ApJS, 254, 39
Gustafsson B., Edvardsson B., Eriksson K., Jørgensen U. G., Nordlund Å., Plez B., 2008, A&A, 486, 951
Guzmán-Mesa A. et al., 2020, AJ, 160, 15
Hakim K., Rivoldini A., Van Hoolst T., Cottenier S., Jaeken J., Chust T., Steinle-Neumann G., 2018, Icarus, 313, 61
Haldemann J., Alibert Y., Mordasini C., Benz W., 2020, A&A, 643, A105
Hayward T. L., Brandl B., Pirger B., Blacken C., Gull G. E., Schoenwald J., Houck J. R., 2001, PASP, 113, 105
Hébrard G. et al., 2008, A&A, 488, 763
Hébrard G. et al., 2016, A&A, 588, A145
Heiter U. et al., 2021, A&A, 645, A106
Howell S. B., Furlan E., 2022, Front. Astron. Space Sci., 9, 871163
Howell S. B., Everett M. E., Sherry W., Horch E., Ciardi D. R., 2011, AJ, 142, 19

Howell S. B., Scott N. J., Matson R. A., Everett M. E., Furlan E., Gnilka C. L., Ciardi D. R., Lester K. V., 2021, Front. Astron. Space Sci., 8, 10
Hoyer S., Guterman P., Demangeon O., Sousa S. G., Deleuil M., Meunier J. C., Benz W., 2020, A&A, 635, A24
Huang C. X. et al., 2020, Res. Notes Am. Astron. Soc., 4, 206
Jenkins J. M., 2002, ApJ, 575, 493
Jenkins J. M. et al., 2010, in Radziwill N. M., Bridger A., eds, Proc. SPIE Conf. Ser. Vol. 7740, Software and Cyberinfrastructure for Astronomy. SPIE, Bellingham, p. 77400D
Jenkins J. M. et al., 2016, in Chiozzi G., Guzman J. C., eds, Proc. SPIE Conf. Ser. Vol. 9913, Software and Cyberinfrastructure for Astronomy IV. SPIE, Bellingham, p. 1232
Jenkins J. M., Tenenbaum P., Seader S., Burke C. J., McCauliff S. D., Smith J. C., Twicken J. D., Chandrasekaran H., 2020, Kepler Data Processing Handbook: Transiting Planet Search, Kepler Science Document KSCI-19081-003
Jensen E., 2013, Tapir: A web interface for transit/eclipse observability, Astrophysics Source Code Library, record ascl:1306.007
Kempton E. M. R. et al., 2018, PASP, 130, 114401
Kipping D. M., 2013, MNRAS, 434, L51
Kipping D., 2018, Res. Notes Am. Astron. Soc., 2, 223
Kurucz R. L., 1992, in Barbuy B., Renzini A., eds, Proc. IAU Symp. 149, The Stellar Populations of Galaxies. Springer, Dordrecht, p. 225
Kurucz R. L., 1993, SYNTHE Spectrum Synthesis Programs and Line Data. Astrophysics Source Code Library
Leleu A. et al., 2021, A&A, 649, A26
Lester K. V. et al., 2021, AJ, 162, 75
Li J., Tenenbaum P., Twicken J. D., Burke C. J., Jenkins J. M., Quintana E. V., Rowe J. F., Seader S. E., 2019, PASP, 131, 024506
Lillo-Box J. et al., 2020, MNRAS, 491, 4496
Lindegren L. et al., 1997, A&A, 323, 49
Lindegren L. et al., 2021, A&A, 649, A4
Lissauer J. J. et al., 2012, ApJ, 750, 112
Lopez E. D., Fortney J. J., 2014, ApJ, 792, 1
Lubin J. et al., 2022, AJ, 163, 101
McCully C., Volgenau N. H., Harbeck D.-R., Lister T. A., Saunders E. S., Turner M. L., Siiverd R. J., Bowman M., 2018, in Guzman J. C., Ibsen J., eds, Proc. SPIE Conf. Ser. Vol. 10707, Software and Cyberinfrastructure for Astronomy V. SPIE, Bellingham, p. 107070K
Mamajek E. E., Hillenbrand L. A., 2008, ApJ, 687, 1264
Masseron T., Merle T., Hawkins K., 2016, BACCHUS: Brussels Automatic Code for Characterizing High accUracy Spectra, record ascl:1605.004
Matson R. A., Howell S. B., Ciardi D. R., 2019, AJ, 157, 211
Maxted P. F. L. et al., 2022, MNRAS, 514, 77
Mugrauer M., Michel K.-U., 2020, Astron. Nachr., 341, 996
Mugrauer M., Michel K.-U., 2021, Astron. Nachr., 342, 840
Noyes R. W., Hartmann L. W., Baliunas S. L., Duncan D. K., Vaughan A. H., 1984, ApJ, 279, 763
Orell-Miquel J. et al., 2023, A&A, 669, A40
Osborn H. P., 2022, MonoTools: Planets of uncertain periods detector and modeler, Astrophysics Source Code Library, record ascl:2204.020
Osborn H. P. et al., 2022, A&A, 664, A156
Owen J. E., 2019, Annu. Rev. Earth Planet. Sci., 47, 67
Pecaut M. J., Mamajek E. E., 2013, ApJS, 208, 9
Perruchot S. et al., 2008, in McLean I. S., Casali M. M., eds, Proc. SPIE Conf. Ser. Vol. 7014, Ground-based and Airborne Instrumentation for Astronomy II. SPIE, Bellingham, p. 70140J
Pollacco D. et al., 2008, MNRAS, 385, 1576
Ricker G. R. et al., 2015, J. Astron. Telesc. Instrum. Syst., 1, 014003
Rodrigues T. S. et al., 2014, MNRAS, 445, 2758
Rodrigues T. S. et al., 2017, MNRAS, 467, 1433
Safonov B. S., Lysenko P. A., Dodin A. V., 2017, Astron. Lett., 43, 344
Salvatier J., Wiecki T. V., Fonnesbeck C., 2016, PeerJ Comput. Sci., 2, e55
Schanche N. et al., 2020, MNRAS, 499, 428
Schanche N. et al., 2022, A&A, 657, A45
Scott N. J. et al., 2021, Front. Astron. Space Sci., 8, 138
Serrano L. M. et al., 2022, A&A, 667, A1
Sheather S. J., Jones M. C., 1991, J. R. Stat. Soc. B, 53, 683

Skrutskie M. F. et al., 2006, AJ, 131, 1163

Smith J. C. et al., 2012, PASP, 124, 1000

Sotin C., Grasset O., Mocquet A., 2007, Icarus, 191, 337

Stassun K. G. et al., 2019, AJ, 158, 138

Stumpe M. C. et al., 2012, PASP, 124, 985

Stumpe M. C., Smith J. C., Catanzarite J. H., Van Cleve J. E., Jenkins J. M., Twicken J. D., Girouard F. R., 2014, PASP, 126, 100

Szabó G. M. et al., 2022, A&A, 659, L7

Tayar J., Claytor Z. R., Huber D., van Saders J., 2022, ApJ, 927, 31

Telting J. H. et al., 2014, Astron. Nachr., 335, 41

The JWST Transiting Exoplanet Community Early Release Science Team, 2023, Nature, 614, 649

Thiabaud A., Marboeuf U., Alibert Y., Cabral N., Leya I., Mezger K., 2014, A&A, 562, A27

Thiabaud A., Marboeuf U., Alibert Y., Leya I., Mezger K., 2015, A&A, 574, A138

Tokovinin A., 2018, PASP, 130, 035002

Tuson A. et al., 2023, MNRAS, 523, 3090

Twicken J. D. et al., 2018, PASP, 130, 064502

Ulmer-Moll S. et al., 2022, A&A, 666, A46

Ulmer-Moll S. et al., 2023, A&A, 674, A43

Van Eylen V. et al., 2019, AJ, 157, 61

Vanderburg A. et al., 2019, ApJ, 881, L19

Waskom M. L., 2021, J. Open Source Softw., 6, 3021

Wizinowich P. et al., 2000, PASP, 112, 315

Wright E. L. et al., 2010, AJ, 140, 1868

Zechmeister M. et al., 2018, A&A, 609, A12

Ziegler C., Tokovinin A., Briceño C., Mang J., Law N., Mann A. W., 2020, AJ, 159, 19

APPENDIX A: DETAILED DESCRIPTION OF HIGH-RESOLUTION IMAGING OBSERVATIONS

A0.1 Keck and Palomar

The Keck Observatory observations were made with the NIRC2 instrument on Keck-II behind the natural guide star AO system (Wizinowich et al. 2000) on 2020 May 28 UT in a standard 3-point dither pattern that is used with NIRC2 to avoid the left lower quadrant of the detector which shows excess noise. The dither pattern step size was 3 arcsec and was repeated twice, with each dither offset from the previous dither by 0.5 arcsec. NIRC2 was used in the narrow-angle mode with a full field of view of ∼10 arcsec and a pixel scale of approximately 0.0099442 arcsec per pixel. The Keck observations were made in the narrow-band filters $Br - \gamma$ filter ($\lambda_o = 2.1686$; $\Delta\lambda = 0.0326\,\mu m$) with an integration time of 2 s for a total of 18 s on target.

The Palomar Observatory observations of HIP 9618 were made with the PHARO instrument (Hayward et al. 2001) behind the natural guide star AO system P3K (Dekany et al. 2013) on 2020 December 4 in a standard 5-point `quincunx` dither pattern with steps of 5 arcsec in the narrow-band $Br - \gamma$ filter ($\lambda_o = 2.1686$; $\Delta\lambda = 0.0326\,\mu m$). Each dither position was observed three times, offset in position from each other by 0.5 arcsec for a total of 15 frames; with an integration time of 1.4 s per frame, respectively for total on-source times of 21 s. PHARO has a pixel scale of 0.025 arcsec per pixel for a total field of view of ∼25 arcsec.

Palomar and Keck data were processed and analysed with a custom set of IDL tools. The science frames were flat-fielded and sky-subtracted. The flat fields were generated from a median average of dark subtracted flats taken on-sky. The flats were normalized such that the median value of the flats is unity. The sky frames were generated from the median average of the dithered science frames; each science image was then sky-subtracted and flat-fielded. Reduced
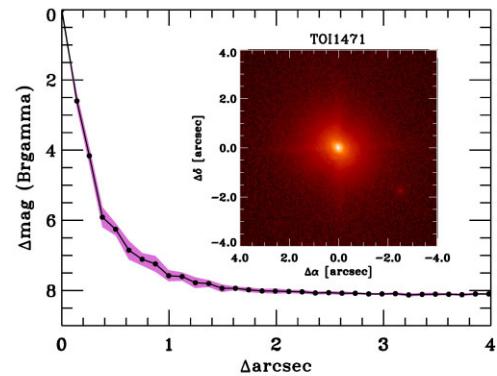
(a) Palomar NIR AO imaging and sensitivity curve for HIP 9618 (or TOI-1471) taken in the Brγ filter. The image reaches a contrast of ∼ 7 magnitudes fainter than the host star within 0."5. *Inset:* Image of the central portion of the data, centered on the star and showing the faint background star 3″ to the southwest.
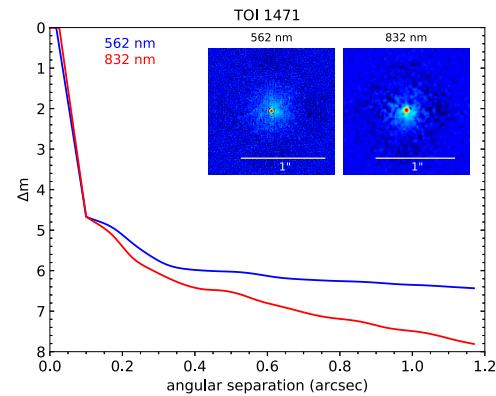
(b) We show the 5σ speckle imaging contrast curves in both filters as a function of the angular separation from the diffraction limit out to 1.2 arcsec. The inset shows the reconstructed 832 nm image with a 1 arcsec scale bar. The star, HIP 9618 or TOI1471, was found to have no close companions to within the angular and contrast levels achieved.
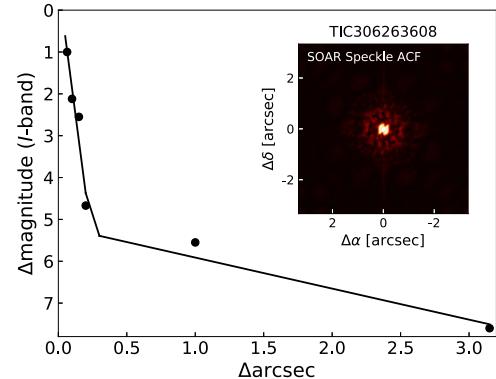
(c) Similar to above, the speckle imaging contrast curve from the SOAR telescope taken in visible I-band filter. The inset shows the speckle auto-correlation function, showing no nearby star within the sensitivity of the observation.

Figure A1. High-resolution imaging results.

science frames were combined into a single combined image using a intrapixel interpolation that conserves flux, shifts the individual dithered frames by the appropriate fractional pixels, and median-coadds the frames. The final resolutions of the combined dithers were determined from the full-width half-maximum of the point spread functions: 0.12 arcsec and 0.078 arcsec for the Palomar and Keck observations, respectively.

The sensitivities of the final combined AO image were determined by injecting simulated sources azimuthally around the primary target every 20° at separations of integer multiples of the central source's FWHM (Furlan et al. 2017). The brightness of each injected source was scaled until standard aperture photometry detected it with 5σ significance. The resulting brightness of the injected sources relative to HIP 9618 set the contrast limits at that injection location. The final 5σ limit at each separation was determined from the average of all of the determined limits at that separation and the uncertainty on the limit was set by the rms dispersion of the azimuthal slices at a given radial distance. The Keck data have better sensitivity closer-in (δmag = 2.5 mag at 0.1 arcsec), but the Palomar data are deeper sensitivity at wider separations (δmag = 8 mag at 2 arcsec); the final sensitivity curves for the Palomar is shown in Fig. A1(a).

A0.2 Gemini

TOI-1471 was observed on 2020 December 4 UT and 2021 October 17 UT using the 'Alopeke speckle instrument on the Gemini North 8-m telescope (Scott et al. 2021; Howell & Furlan 2022). 'Alopeke provides simultaneous speckle imaging in two bands (562 and 832 nm) with output data products including a reconstructed image with robust contrast limits on companion detections. While both observations had consistent results that TOI-1471 is a single star to within the angular and contrast levels achieved, the 2021 October observation had better seeing which led to deeper contrast levels. Twelve sets of 1000 × 0.06 s images were obtained and processed in our standard reduction pipeline (Howell et al. 2011). Fig. A1(b) shows our final contrast curves and the 832 nm reconstructed speckle

image. We find that TOI-1471 is a single star with no companion brighter than 5–8 magnitudes below that of the target star from the 8-m telescope diffraction limit (20 mas) out to 1.2 arcsec. At the distance of TOI-1471 ($d = 67.5$ pc) these angular limits correspond to spatial limits of 1.35–81 au.

A0.3 SOAR

We searched for nearby stellar companions to TOI-1471 with speckle imaging on the 4.1-m Southern Astrophysical Research (SOAR) telescope (Tokovinin 2018) on 2020 October 31 UT, observing in Cousins *I*-band, a similar visible bandpass as *TESS*. This observation was sensitive to a 7.6-magnitude fainter star at an angular distance of 1 arcsec from the target. More details of the observations within the SOAR *TESS* survey are available in Ziegler et al. (2020). The 5σ detection sensitivity and speckle autocorrelation functions from the observations are shown in Fig. A1(c). No nearby stars were detected within 3 arcsec of TOI-1471 in the SOAR observations.

A0.4 SAI-2.5m

We also observed TOI-1471 on 2020 December 3 UT with the SPeckle Polarimeter Safonov et al. (SPP 2017) on the 2.5 m telescope at the Caucasian Observatory of Sternberg Astronomical Institute (SAI) of Lomonosov Moscow State University in the spectral band centred on 625 nm with FWHM of 50 nm. SPP uses an Electron Multiplying CCD Andor iXon 897 as a detector, and we used the atmospheric dispersion compensation. The detector has a pixel scale of 20.6 mas pixel^{-1}, the angular resolution is 89 mas, and the field of view is 5 arcsec × 5 arcsec centred on the star. The power spectrum was estimated from 4000 frames with 30 ms exposures. We did not detect any stellar companions brighter than Δmag = 4.3 and 6.2 at 0.2 arcsec and 0.5 arcsec, respectively.

APPENDIX B: RV OBSERVATIONS

Table B1. Radial velocities and spectral activity indicators measured from TNG/HARPS-N spectra with the DRS.

BJD$_{TBD}$ -2457000	RV (m s^{-1})	σ_{RV} (m s^{-1})	BIS (m s^{-1})	σ_{BIS} (m s^{-1})	CCF_FWHM (km s^{-1})	CCF_CTR (per cent)	log R$'_{HK}$ –	$\sigma_{\log R'_{HK}}$ –	SNR@550nm (@550nm)	T_{exp} (s)
1869.31908	−16047.975	1.897	−27.281	2.682	6.780	47.865	−4.9633	0.0205	47.9	281.1
1869.33575	−16033.064	0.784	−25.601	1.109	6.779	47.942	−4.9847	0.0060	105.3	1500.0
1895.39675	−16042.441	1.373	−27.726	1.941	6.781	48.022	−5.0056	0.0160	63.7	1500.0
1896.38630	−16040.879	1.049	−24.883	1.484	6.787	47.982	−4.9759	0.0097	81.1	1500.0
1897.38259	−16041.553	0.938	−22.277	1.326	6.777	47.980	−4.9577	0.0078	90.5	1500.0
1898.38722	−16040.521	0.783	−25.694	1.108	6.783	47.944	−4.9640	0.0059	107.3	1500.0
1905.36412	−16043.817	1.567	−28.000	2.216	6.778	47.951	−4.9860	0.0191	57.5	1723.9
2548.36087	−16080.145	1.945	−33.469	2.750	6.768	48.124	−5.0687	0.0392	51.1	2400.0
2574.43126	−16091.191	4.260	−35.382	6.024	6.777	47.795	−4.8758	0.0726	28.4	680.8
2574.45186	−16081.583	1.483	−32.075	2.098	6.768	47.980	−4.9197	0.0205	66.6	1800.0
2594.45356	−16081.331	1.521	−29.413	2.151	6.769	47.996	−4.9653	0.0215	63.3	1200.0
2609.38503	−16085.546	2.553	−29.236	3.610	6.776	48.181	−5.0135	0.0504	40.9	600.0
2610.39501	−16082.079	1.138	−33.068	1.609	6.772	48.079	−4.9536	0.0119	81.8	600.0

Table B2. *SOPHIE* radial velocities.

BJD [JD-2400000]	RV (m s^{-1})	σ_{RV} (m s^{-1})
55853.53644	−15914.0	2.5
55883.46881	−15930.8	2.7
55916.41221	−15914.6	3.2
58840.4519	−16074.0	3.7
58841.37571	−16071.4	3.9
58857.29082	−16070.8	3.8
58858.37755	−16077.1	3.8
58887.31391	−16044.8	3.8
59057.60564	−16085.0	1.6
59058.60044	−16084.1	3.9
59060.60405	−16100.6	3.8
59063.63157	−16074.4	3.8
59082.57844	−16072.7	3.8
59112.60148	−16094.3	3.9
59113.64083	−16067.6	3.7
59134.53817	−16076.2	3.8
59138.52924	−16081.4	3.8
59139.49069	−16088.6	3.7
59141.49017	−16076.4	3.8
59141.49331	−16070.1	3.8
59146.51885	−16087.6	2.4
59151.48282	−16081.6	2.4
59170.48772	−16092.2	2.4
59457.6237	−16119.7	2.4
59527.52674	−16110.2	2.4
59542.47712	−16113.9	2.4
59565.33575	−16114.2	2.4

Table B3. *CAFE* radial velocities.

BJD	RV (m s^{-1})	σ_{RV} (m s^{-1})
2459529.4721648	−16184.7	9.9
2459530.4696387	−16228.9	8.2
2459549.4579368	−16231.9	7.0
2459577.4456190	−16212.1	5.7
2459578.4636742	−16229.2	6.1
2459617.3591001	−16201.4	6.5
2459808.6769329	−16200.3	5.4
2459809.6736999	−16206.2	5.4
2459810.6673429	−16225.4	5.9

APPENDIX C: MODEL PRIORS AND POSTERIORS

APPENDIX D: INTERIOR COMPOSITION

Table C1. Model parameters, priors, and posteriors for the combined model.

Parameter	Prior	Posterior
Stellar temperature, $T_{\rm eff}$ (K)	$\mathcal{N}(\mu = 5610, \sigma = 30)$	5609.0 ± 33.0
Stellar radius, R_s [$R_\oplus$]	$\mathcal{N}(\mu = 0.9662, \sigma = 0.005)$	0.9662 ± 0.005
log stellar surface gravity, $\log g$ (cgs)	$\mathcal{N}(\mu = 4.47, \sigma = 0.1)$	$4.45^{+0.016}_{-0.033}$
Log radius ratio, $\log R_{p,b}/R_s$, b	$\mathcal{U}(a = -6.908, b = -2.303)$	-3.297 ± 0.01
Log radius ratio, $\log R_{p,c}/R_s$, c	$\mathcal{U}(a = -6.908, b = -2.303)$	-3.451 ± 0.011
Impact parameter, b_b	$\mathcal{U}(a = 0.0, b = 1 + R_{p,b}/R_s)^\dagger$	0.13 ± 0.11
Impact parameter, b_c	$\mathcal{U}(a = 0.0, b = 1 + R_{p,c}/R_s)^\dagger$	$0.235^{+0.085}_{-0.062}$
RV semi-amplitude, K_b (m s^{-1}), b	$\mathcal{U}(a = -10, b = 10)$	2.48 ± 0.71
RV semi-amplitude, K_c (m s^{-1}), c	$\mathcal{U}(a = -10, b = 10)$	1.39 ± 0.58
Quadratic LD, $u_{\rm TESS,\,0}$	$\mathcal{N_U}(a = 0.0, b = 1.0, \mu = 0.3299, \sigma = 0.0500)$	0.302 ± 0.061
Quadratic LD, $u_{\rm TESS,\,1}$	$\mathcal{N_U}(a = 0.0, b = 1.0, \mu = 0.2605, \sigma = 0.0500)$	0.223 ± 0.086
Quadratic LD, $u_{\rm Cheops,\,0}$	$\mathcal{N_U}(a = 0.0, b = 1.0, \mu = 0.4494, \sigma = 0.0500)$	0.501 ± 0.064
Quadratic LD, $u_{\rm Cheops,\,1}$	$\mathcal{N_U}(a = 0.0, b = 1.0, \mu = 0.2292, \sigma = 0.0500)$	0.174 ± 0.082
Eccentricity, e_b	$\mathcal{B}(\alpha = 0.867, \beta = 3.03)^\ddagger$	$0.22^{+0.25}_{-0.15}$
Eccentricity, e_c	$\mathcal{B}(\alpha = 0.867, \beta = 3.03)^\ddagger$	$0.23^{+0.25}_{-0.16}$
Argument of periastron, ω_b,	$\mathcal{U}(a = -\pi, b = \pi)$	0.0 ± 3.9
Argument of periastron, ω_c,	$\mathcal{U}(a = -\pi, b = \pi)$	0.1 ± 3.9
SOPHIE RV mean, $\mu_{\rm SOPHIE}$	$\mathcal{N}(\mu = -16077.1, \sigma = 53.265)$	-16084.7 ± 1.9
HARPS-N RV mean, $\mu_{\rm HARPS\text{-}N}$	$\mathcal{N}(\mu = -2.8479, \sigma = 10.7575)$	-14.16 ± 0.36
CAFE RV mean, $\mu_{\rm CAFE}$	$\mathcal{N}(\mu = -16212.1, \sigma = 96.2822)$	-16178.4 ± 7.1
RV quadratic trend, (m s^{-1} d^{-2})	$\mathcal{N}(\mu = 0, \sigma = 0.005)$	$-4.99e - 06 \pm 6.4e - 07$
RV linear trend, (m s^{-1} d^{-1})	$\mathcal{N}(\mu = 0, \sigma = 0.05)$	-0.0666 ± 0.0013
log RV scatter, $\log \sigma_{\rm SOPHIE}$	$\mathcal{N}(\mu = 2.15791, \sigma = 2)$	2.13 ± 0.17
log RV scatter, $\log \sigma_{\rm HARPS\text{-}N}$	$\mathcal{N}(\mu = -1.88719, \sigma = 2)$	$-2.2^{+1.5}_{-1.9}$
log RV scatter, $\log \sigma_{\rm CAFE}$	$\mathcal{N}(\mu = 2.84818, \sigma = 2)$	2.98 ± 0.29
Log photometric scatter, $\log \sigma_{\rm TESS,s}$/(ppt)	$\mathcal{N}(\mu = 0.1435, \sigma = 3)$	0.1 ± 3.0
I mag contamination from companion, ΔI	$\mathcal{N}(\mu = 7.398, \sigma = 1.767)$	7.4 ± 1.7
Log photometric scatter, $\log \sigma_{\rm Cheops,s}$/(ppt)	$\mathcal{N}(\mu = -7.605, \sigma = 3)$	-7.5 ± 3.0
V mag contamination from companion, ΔV	$\mathcal{N}(\mu = 8.966, \sigma = 2.076)$	9.0 ± 2.1
Correlation with normalized background flux, $df/d(\cos((BG - \mu_{\rm BG})/\sigma_{\rm BG}))$	$\mathcal{N}(\mu = 0, \sigma = 0.4474)$	-0.09 ± 0.1
Correlation with normalized sine of roll angle, $df/d(\sin((\Phi - \mu_\Phi)/\sigma_\Phi))$	$\mathcal{N}(\mu = 0, \sigma = 0.4474)$	0.002 ± 0.048
Correlation with normalized cosine of roll angle, $df/d(\cos((\Phi - \mu_\Phi)/\sigma_\Phi))$	$\mathcal{N}(\mu = 0, \sigma = 0.4474)$	0.125 ± 0.047
CHEOPS linear trend for fk = PR110048_TG017201_V0200	$\mathcal{N}(\mu = 0, \sigma = 0.852144)$	-0.042 ± 0.044
CHEOPS offset for fk = PR110048_TG017201_V0200	$\mathcal{N}(\mu = 0, \sigma = 0.313486)$	0.01 ± 0.13
CHEOPS linear trend for fk = PR110048_TG017301_V0200	$\mathcal{N}(\mu = 0, \sigma = 0.852144)$	0.009 ± 0.035
CHEOPS offset for fk = PR110048_TG017301_V0200	$\mathcal{N}(\mu = 0, \sigma = 0.313486)$	-0.02 ± 0.13
CHEOPS linear trend for fk = PR110048_TG017401_V0200	$\mathcal{N}(\mu = 0, \sigma = 0.852144)$	-0.132 ± 0.038
CHEOPS offset for fk = PR110048_TG017401_V0200	$\mathcal{N}(\mu = 0, \sigma = 0.313486)$	-0.02 ± 0.13
CHEOPS linear trend for fk = PR110048_TG017601_V0200	$\mathcal{N}(\mu = 0, \sigma = 0.852144)$	-0.061 ± 0.035
CHEOPS offset for fk = PR110048_TG017601_V0200	$\mathcal{N}(\mu = 0, \sigma = 0.313486)$	-0.02 ± 0.13
BSpline 1, $F(\Phi)_{\rm BS,\,1}$	$\mathcal{N}(\mu = 0.0, \sigma = 0.0)$	0.153 ± 0.096
BSpline 2, $F(\Phi)_{\rm BS,\,2}$	$\mathcal{N}(\mu = 0.0, \sigma = 0.0)$	-0.004 ± 0.096
BSpline 3, $F(\Phi)_{\rm BS,\,3}$	$\mathcal{N}(\mu = 0.0, \sigma = 0.0)$	$0.014^{+0.095}_{-0.095}$
BSpline 4, $F(\Phi)_{\rm BS,\,4}$	$\mathcal{N}(\mu = 0.0, \sigma = 0.0)$	0.061 ± 0.088
BSpline 5, $F(\Phi)_{\rm BS,\,5}$	$\mathcal{N}(\mu = 0.0, \sigma = 0.0)$	-0.03 ± 0.084
BSpline 6, $F(\Phi)_{\rm BS,\,6}$	$\mathcal{N}(\mu = 0.0, \sigma = 0.0)$	-0.14 ± 0.079
BSpline 7, $F(\Phi)_{\rm BS,\,7}$	$\mathcal{N}(\mu = 0.0, \sigma = 0.0)$	$-0.09^{+0.075}_{-0.074}$
BSpline 8, $F(\Phi)_{\rm BS,\,8}$	$\mathcal{N}(\mu = 0.0, \sigma = 0.0)$	-0.049 ± 0.071
BSpline 9, $F(\Phi)_{\rm BS,\,9}$	$\mathcal{N}(\mu = 0.0, \sigma = 0.0)$	0.087 ± 0.071
BSpline 10, $F(\Phi)_{\rm BS,\,10}$	$\mathcal{N}(\mu = 0.0, \sigma = 0.0)$	-0.003 ± 0.072
BSpline 11, $F(\Phi)_{\rm BS,\,11}$	$\mathcal{N}(\mu = 0.0, \sigma = 0.0)$	0.057 ± 0.074
BSpline 12, $F(\Phi)_{\rm BS,\,12}$	$\mathcal{N}(\mu = 0.0, \sigma = 0.0)$	-0.028 ± 0.077
BSpline 13, $F(\Phi)_{\rm BS,\,13}$	$\mathcal{N}(\mu = 0.0, \sigma = 0.0)$	0.029 ± 0.08
BSpline 14, $F(\Phi)_{\rm BS,\,14}$	$\mathcal{N}(\mu = 0.0, \sigma = 0.0)$	-0.019 ± 0.089
BSpline 15, $F(\Phi)_{\rm BS,\,15}$	$\mathcal{N}(\mu = 0.0, \sigma = 0.0)$	$0.065^{+0.095}_{-0.093}$
BSpline 16, $F(\Phi)_{\rm BS,\,16}$	$\mathcal{N}(\mu = 0.0, \sigma = 0.0)$	-0.12 ± 0.11

Note. $\mathcal{N}$ details a normally distributed prior with mean, μ and standard deviation, σ values. $\mathcal{U}$ details a uniform distribution with lower, a, and upper, b, limits. $\mathcal{N_U}$ details a truncated normal distribution with μ, σ, a, and b values.$\dagger$ represents the Espinoza (2018) prior and $\ddagger$ represents the uniform prior as presented by Espinoza (2018) and implemented by `exoplanet`. $\ddagger$ is the prior from Kipping (2013) *CHEOPS* suffixes refer chronologically to the four unique *CHEOPS* visits.
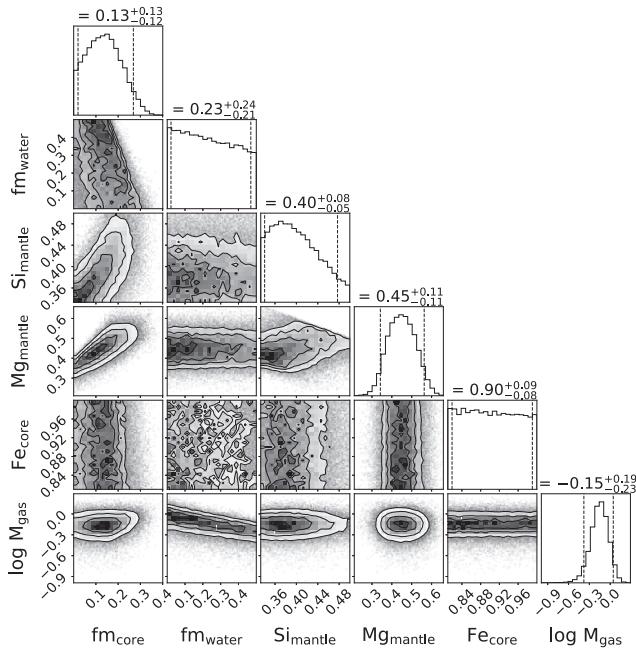
Figure D1. Corner plot showing the posterior distributions of the main internal structure parameters of HIP 9618 b: The layer mass fractions of the inner iron core and the water layer (both with respect to the solid planet without the gas layer), the molar fractions of Si and Mg in the mantle and Fe in the iron core and the total gas mass of the planet in Earth masses on a logarithmic scale. The titles of each column correspond to the median and the 5 and 95 percentiles, which are also shown with the dashed lines.

[1]*Physikalisches Institut, University of Bern, Gesellsschaftstrasse 6, CH-3012 Bern, Switzerland*

[2]*Department of Physics and Kavli Institute for Astrophysics and Space Research, Massachusetts Institute of Technology, Cambridge, MA 02139, USA*

[3]*Institute of Astronomy, Faculty of Physics, Astronomy and Informatics, Nicolaus Copernicus University, Grudziądzka 5, PL-87-100 Toruń, Poland*

[4]*Instituto de Astrofísica de Canarias, C/ vía Láctea, s/n, E-38205 La Laguna, Tenerife, Spain*

[5]*Departamento de Astrofísica, Universidad de La Laguna, Av. Astrofísico Francisco Sánchez, s/n, E-38206 La Laguna, Tenerife, Spain*

[6]*Institut d'astrophysique de Paris, UMR7095 CNRS, Université Pierre & Marie Curie, 98bis boulevard Arago, F-75014 Paris, France*

[7]*Centro de Astrobiología (CAB,CSIC-INTA), Dep. de Astrofísica, ESAC campus, Villanueva de la Cañada, E-28692 Madrid, Spain*

[8]*Observatoire Astronomique de l'Université de Genève, Chemin Pegasi 51, CH-1290 Versoix, Switzerland*

[9]*Department of Astronomy, Stockholm University, AlbaNova University Center, SE-10691 Stockholm, Sweden*

[10]*LAM, Aix Marseille Univ, CNRS, CNES, 13388 Marseille, France*

[11]*Instituto de Astrofísica e Ciências do Espaço, Universidade do Porto, CAUP, Rua das Estrelas, P-4150-762 Porto, Portugal*

[12]*Center for Astrophysics, Harvard and Smithsonian, 60 Garden Street, Cambridge, MA 02138, USA*

[13]*INAF, Osservatorio Astronomico di Padova, Vicolo dell'Osservatorio 5, I-35122 Padova, Italy*

[14]*NASA Exoplanet Science Institute-Caltech/IPAC, Pasadena, CA 91125, USA*

[15]*Centre for Exoplanet Science, SUPA School of Physics and Astronomy, University of St Andrews, North Haugh, St Andrews KY16 9SS, UK*

[16]*Dipartimento di Fisica, Universita degli Studi di Torino, via Pietro Giuria 1, I-10125 Torino, Italy*

[17]*Astrophysics Group, Cavendish Laboratory, University of Cambridge, J.J. Thomson Avenue, Cambridge CB3 0HE, UK*

[18]*Max-Planck-Institut für Astronomie, Königstuhl 17, D-69117 Heidelberg, Germany*

[19]*Department of Physics, Engineering and Astronomy, Stephen F. Austin State University, 1936 North St, Nacogdoches, TX 75962, USA*

[20]*Institut de Ciencies de l'Espai (ICE, CSIC), Campus UAB, Can Magrans s/n, E-08193 Bellaterra, Spain*

[21]*Institut d'Estudis Espacials de Catalunya (IEEC), E-08034 Barcelona, Spain*

[22]*Observatoire de Haute-Provence, CNRS, Université d'Aix-Marseille, F-04870 Saint-Michel-l'Observatoire, France*

[23]*European Space Agency (ESA), European Space Research and Technology Centre (ESTEC), Keplerlaan 1, NL-2201 AZ Noordwijk, the Netherlands*

[24]*Depto. de Astrofisica, Centro de Astrobiologia (CSIC-INTA), ESAC campus, E-28692 Villanueva de la Cañada (Madrid), Spain*

[25]*Space Research Institute, Austrian Academy of Sciences, Schmiedlstrasse 6, A-8042 Graz, Austria*

[26]*Sternberg Astronomical Institute Lomonosov Moscow State University, Universitetskii prospekt, 13, Moscow 119992, Russia*

[27]*Center for Space and Habitability, University of Bern, Gesellsschaftsstrasse 6, CH-3012 Bern, Switzerland*

[28]*Max Planck Institute for Extraterrestrial Physics,*

[29]*Université Grenoble Alpes, CNRS, IPAG, F-38000 Grenoble, France*

[30]*1DTU Space, National Space Institute, Technical University of Denmark, Elektrovej 328, DK-2800 Kgs. Lyngby, Denmark*

[31]*Admatis, 5. Kandó Kálmán Street, 3534 Miskolc, Hungary*

[32]*Instituto de Astrofisica e Ciencias do Espaco, Universidade do Porto, CAUP, Rua das Estrelas, P-4150-762 Porto, Portugal*

[33]*Departamento de Fisica e Astronomia, Faculdade de Ciencias, Universidade do Porto, Rua do Campo Alegre, P-4169-007 Porto, Portugal*

[34]*Institute of Planetary Research, German Aerospace Center (DLR), Rutherfordstrasse 2, D-12489 Berlin, Germany*

[35]*Université de Paris, Institut de physique du globe de Paris, CNRS, F-75005 Paris, France*

[36]*Centre for Mathematical Sciences, Lund University, Box 118, SE-22100 Lund, Sweden*

[37]*Université Grenoble Alpes, CNRS, IPAG, F-38000 Grenoble, France*

[38]*Astrobiology Research Unit, Université de Liège, Allée du 6 Août 19C, B-4000 Liège, Belgium*

[39]*Space Sciences, Technologies and Astrophysics Research (STAR) Institute, Université de Liège, 19C Allée du 6 Août, B-4000 Liège, Belgium*

[40]*Center for Space and Habitability, Gesellsschaftsstrasse 6, CH-3012 Bern, Switzerland*

[41]*Lunar and Planetary Laboratory, The University of Arizona, Tucson, AZ 85721, USA*

[42]*Leiden Observatory, University of Leiden, PO Box 9513, NL-2300 RA Leiden, the Netherlands*

[43]*Department of Space, Earth and Environment, Chalmers University of Technology, Onsala Space Observatory, SE- 43992 Onsala, Sweden*

[44]*Department of Astronomy and Astrophysics, University of California, Santa Cruz, CA 95064, USA*

[45]*Department of Astrophysics, University of Vienna, Tuerkenschanzstrasse 17, A-1180 Vienna, Austria*

[46]*NASA Ames Research Center, Moffett Field, CA 94035, USA*

[47]*LESIA, Observatoire de Paris, Université PSL, Sorbonne Université, Université Paris Cité, CNRS, 5 place Jules Janssen, F-92195 Meudon, France*

[48]*Konkoly Observatory, Research Centre for Astronomy and Earth Sciences, 1121 Budapest, Konkoly Thege Miklós út 15-17, Hungary*

[49]*ELTE Eötvös Loránd University, Institute of Physics, Pázmány Péter sétány 1/A, 1117 Budapest, Hungary*

[50]*Department of Space, Earth and Environment, Astronomy and Plasma Physics, Chalmers University of Technology, SE-412 96 Gothenburg, Sweden*

[51]*Lund Observatory, Division of Astrophysics, Department of Physics, Lund University, Box 43, SE-22100 Lund, Sweden*

[52]*Astrophysics Group, Keele University, Staffordshire ST5 5BG, UK*

[53]*IMCCE, UMR8028 CNRS, Observatoire de Paris, PSL Univ., Sorbonne Univ., 77 av. Denfert-Rochereau, F-75014 Paris, France*

[54]*Institut d'astrophysique de Paris, UMR7095 CNRS, Université Pierre & Marie Curie, 98bis blvd. Arago, F-75014 Paris, France*
[55]*Department of Astronomy and Astrophysics, University of Chicago, Chicago, IL 60637, USA*
[56]*Laboratório Nacional de Astrofísica, Rua Estados Unidos 154, 37504-364 Itajubá-MG, Brazil*
[57]*Space Telescope Science Institute, 3700 San Martin Drive, Baltimore, MD 21218, USA*
[58]*Google, 02142 Cambridge, MA, USA*
[59]*Université de Toulouse, CNRS, IRAP, 14 avenue Belin, F-31400 Toulouse, France*
[60]*Department of Physics and Astronomy, Swarthmore College, Swarthmore, PA 19081, USA*
[61]*INAF, Osservatorio Astrofisico di Catania, Via S. Sofia 78, I-95123 Catania, Italy*
[62]*Dipartimento di Fisica e Astronomia 'Galileo Galilei', Universita degli Studi di Padova, Vicolo dell'Osservatorio 3, I-35122 Padova, Italy*
[63]*Department of Physics, University of Warwick, Gibbet Hill Road, Coventry CV4 7AL, UK*

[64]*Centre for Origin and Prevalence of Life, ETH Zurich, Wolfgang-Pauli-Strasse 27, CH-8093 Zurich, Switzerland*
[65]*Cavendish Laboratory, JJ Thomson Avenue, Cambridge CB3 0HE, UK*
[66]*Center for Astronomy and Astrophysics, Technical University Berlin, Hardenberstrasse 36, D-10623 Berlin, Germany*
[67]*Institut für Geologische Wissenschaften, Freie Universität Berlin, D-12249 Berlin, Germany*
[68]*ELTE Eötvös Loránd University, Gothard Astrophysical Observatory, 9700 Szombathely, Szent Imre h. u. 112, Hungary*
[69]*MTA-ELTE Exoplanet Research Group, 9700 Szombathely, Szent Imre h. u. 112, Hungary*
[70]*German Aerospace Center (DLR), Institute of Optical Sensor Systems, Rutherfordstraße 2, D-12489 Berlin, Germany*
[71]*Institute of Astronomy, University of Cambridge, Madingley Road, Cambridge CB3 0HA, UK*
[72]*Department of Astrophysical Sciences, Princeton University, 4 Ivy Lane, Princeton, NJ 08544, USA*

This paper has been typeset from a TeX/LaTeX file prepared by the author.